Switchable Stiffness Scanning Microscope Probe

by

Clemens T. Mueller-Falcke

B.S., Mechanical Engineering (2000)

Technische Universität Darmstadt

Submitted to the Department of Mechanical Engineering
in Partial Fulfillment of the Requirements for the Degree of
Master of Science in Mechanical Engineering

at the

Massachusetts Institute of Technology

June 2005

© MMV Massachusetts Institute of Technology
All rights reserved.

MASSACHUSETTS INSTITUTE OF TECHNOLOGY
JUN 16 2005
LIBRARIES

Signature of Author . . . . . .
Department of Mechanical Engineering
May 19, 2005

Certified by . . . . . .
Sang-Gook Kim
Associate Professor of Mechanical Engineering
Thesis Supervisor

Accepted by . . . . . .
Lallit Anand
Professor of Mechanical Engineering
Chairman, Department Committee on Graduate Students

BARKER

MIT Libraries
Document Services

Room 14-0551
77 Massachusetts Avenue
Cambridge, MA 02139
Ph: 617.253.2800
Email: docs@mit.edu
http://libraries.mit.edu/docs

DISCLAIMER OF QUALITY

Due to the condition of the original material, there are unavoidable flaws in this reproduction. We have made every effort possible to provide you with the best copy available. If you are dissatisfied with this product and find it unusable, please contact Document Services as soon as possible.

Thank you.

The images contained in this document are of the best quality available.

Switchable Stiffness Scanning Microscope Probe

by

Clemens T. Mueller-Falcke

Submitted to the Department of Mechanical Engineering
on May 20, 2005 in partial fulfillment of the
requirements for the Degree of Master of Science in
Mechanical Engineering

ABSTRACT

Atomic Force Microscopy (AFM) has rapidly gained widespread utilization as an imaging device and micro/nano-manipulator during recent years. This thesis investigates the new concept of a dual stiffness scanning probe with respect to biological applications and determines the resulting requirements for the scanning of soft bio samples, such as low-pressure contact. On this basis, an in-plane AFM probe that is specifically tailored to the needs of biological applications is developed. It features a variable stiffness, which makes the stiffness of the probe adjustable to the surface hardness of the sample, and a very low overall stiffness, which is needed in order to achieve high resolution imaging.

The switchable stiffness probe allows the scanning of biological samples with varying surface hardness without changing probes during scanning, and therefore prevents a loss of positional information, as is unavoidable with conventional devices. For the integration of the components into a MEMS device, the conventional cantilever-type design of AFM probes has been abandoned in favor of an in-plane design. The new design has an advantage in that it facilitates a high-density array of AFM probes and allows for easy surface micromachining of the integrated device. It also enables the future integration of micro-fluidic channels for reagent delivery and nanopipetting. For the scanning of nano-scale trenches and grooves, a multi-walled carbon nanotube, embedded in a nanopellet, is planned as a high-aspect-ratio tip.

The variable stiffness is accomplished in a mechanical way by engaging or disengaging auxiliary beams to the compliant beam structure by means of electrostatically actuated clutches. For actuation, an electrostatic combdrive is considered to move the probe tip up and down. The vertical displacement of the tip can be measured by a capacitive sensor, which can easily be integrated into the system.

A scaled-up proof-of-concept model is manufactured with surface-micromachining processes. The clutch performance is successfully tested and the dual stiffness concept is verified by measuring the stiffness of the device with the clutches engaged and disengaged.

Thesis Supervisor: Sang-Gook Kim
Title: Esther and Harold E. Edgerton Associate Professor of Mechanical Engineering

Acknowledgements

First and foremost, I would like to thank Professor Sang-Gook Kim for his support over the last two years. He has always been inspiring in his ideas and advice, finding the right balance between providing the necessary freedom, keeping me focused, and drawing my attention to the big picture. I am thankful for what I have learned as a part of his research group, the Micro & Nano Systems Laboratory, which was especially fruitful due to the variety of interesting research being conducted.

The manufacturing part of this research required significant experimental work on machines that I knew nothing about prior to starting the project. Yong Shi has been very helpful in getting me started, and I would like to thank him and Yong-Ak Song for advice and comments on the fabrication processes. Also, thanks to Daniel Adams, Robert Bicchieri, Kurt Broderick, Dave Terry, and Paul Tierney, for training and expertise on various equipment at the Microsystems Technology Laboratories.

Finally, I would like to thank Wonjae Choi for keeping me company during many lunch and coffee breaks, and Sunil Gouda, Soohyung Kim, and Hongchul Jang for the great time I had with them.

Contents

1. INTRODUCTION 11

1.1 MOTIVATION 11
1.2 DEVICE DESCRIPTION 13
1.3 COMPETING SOLUTIONS 14
1.4 PURPOSE AND ORGANIZATION OF THE DOCUMENT 14

2. BACKGROUND 16

2.1 CURRENT AFM PRACTICE 16
2.2 AFM APPLICATIONS 17
2.2.1 Biological Applications 18
2.2.2 Special Requirements of Biological Samples 19
2.3 DRAWBACKS OF CONVENTIONAL AFM 21

3. DESIGN PROCESS 23

3.1 FUNCTIONAL REQUIREMENTS AND MAPPING TO DESIGN PARAMETERS 23
3.2 REALIZATION OF THE SWITCHABLE STIFFNESS 24
3.3 DETERMINING OPTIMAL PROBE STIFFNESS 27
3.3.1 Lower limit for the probe stiffness – reasons for choosing a high stiffness 27
3.3.2 Upper limit for the probe stiffness – reasons to choose a low stiffness 30
3.3.3 Choosing the stiffness 34
3.4 TIP DESIGN 35

4. DEVICE DESCRIPTION 39

4.1 OVERVIEW 39
4.2 SENSOR 40
4.3 FINAL DESIGN 40
4.4 STIFFNESS MODEL 41
4.5 PULL-IN VOLTAGE OF THE CLUTCHES 43
4.6 DYNAMIC MODEL AND TESTING 45

5. MANUFACTURING 47

5.1 PROCESS FLOW OVERVIEW 47
5.2 MASK DESIGN 48
5.3 STEP BY STEP FABRICATION PROCESS 50
5.3.1 Alignment Marks 50
5.3.2 SU-8 Structure 51
5.3.3 XeF_2-etch to create undercut 52
5.3.4 Electrodes 53
5.3.5 XeF_2 Release Etch 55
5.4 ISSUES AND CHALLENGES 56
5.4.1 SU-8 56
5.4.2 Electrode Lift-Off 57
5.4.3 XeF_2 Release Etch 57

5.5 RESULTS AND SUMMARY 58

6. DEVICE TESTING AND DISCUSSION 63

6.1 CLUTCH PERFORMANCE 63
6.2 STIFFNESS MEASUREMENT OF THE AFM PROBE 66

7. CONCLUSION AND FUTURE WORK 71

7.1 CONCLUSION 71
7.2 FUTURE WORK 71
7.3 PROMISING APPLICATIONS 72
7.3.1 Protein Printing 72
7.3.2 Tip-enhanced Raman Spectroscopy 74

BIBLIOGRAPHY 77

List of Figures

Figure 1-1: Device design 13
Figure 2-1: Functional overview of a standard AFM system 16
Figure 2-2: Live osteoblast (bone cell) imaged in contact mode under liquid 19
Figure 2-3: Elasticity image of a living fibroblast (NIH3T3) 21
Figure 3-1: Functional requirements and the corresponding design parameters 24
Figure 3-2: Additional beams can be attached with the help of el. actuators ("clutches") 26
Figure 3-3: The "clutches" are moved to the outside of the device 26
Figure 3-4: Plain structure of the AFM probe without sensors, actuators, tip 26
Figure 3-5: Interaction force F as the tip approaches the sample 28
Figure 3-6: Hertz model of the tip and sample indentation depth h 31
Figure 3-7: SEM picture of the tip of carbon nanotubes 31
Figure 3-8: AFM image of a living mouse fibroblast 35
Figure 3-9: CNT as AFM tip 36
Figure 3-10: Nanopellet with carbon nanotube (a) and its assembly into a V-groove (b) 38
Figure 4-1: CAD model of the in-plane AFM probe 39
Figure 4-2: Close up view of the clutch (a: top view, b: 3D view) 40
Figure 4-3: Device design 41
Figure 4-4: Ideal beam with zero slopes at both ends 41
Figure 4-5: Flexure 1 (a) and its lumped model (b) 42
Figure 4-6: Flexure 2 (a) and its lumped model (b) 42
Figure 4-7: Flexure 3 (a) and its lumped model (b) 42
Figure 4-8: 3D-model for the simulation of the pull-in voltage of the electrostatic actuator. 44
Figure 4-9: MEMCAD result for the pull-in voltage of the electrostatic actuator 44
Figure 5-1 : Process flow 48
Figure 5-2: Discrepancy between initial design feature and resulting feature 49
Figure 5-3: The individual devices are clustered in groups of six on 42 dies 49
Figure 5-4: Mask layout for the alignment marks and close-up view of the alignment mark. 50
Figure 5-5: Mask layout of the SU-8 process 51
Figure 5-6: SEM picture of the SU-8 structure of the AFM probe 52
Figure 5-7: Top view of the undercut 53
Figure 5-8: Mask layout for the metal deposition of the electrodes 54
Figure 5-9: Top view of the SU-8 structure with gold electrodes 55
Figure 5-10: SU-8 structure with sloped sidewalls and with perfectly straight sidewalls 56
Figure 5-11: Top view of the unreleased device 58
Figure 5-12: Top view of the unreleased AFM probe 59

Figure 5-13: Top view of one side of the AFM probe 59
Figure 5-14: Detail A from Figure 5-13 above 62
Figure 5-15: Detail B from Figure 5-13 above 60
Figure 5-16: The protrusions are not covered with metal 60
Figure 5-17: Angled picture to reveal the metal sidewall and the undercut 61
Figure 6-1: Microwave probe station used to test the clutch performance 64
Figure 6-2: Clutch disengaged (a) and engaged (b) 65
Figure 6-3: Schematic view of the functional elements of the Hysitron Triboindenter® 66
Figure 6-4: Outside view of the Hysitron Triboindenter® 67
Figure 6-5: Fixture for correct alignment of the AFM probe 68
Figure 6-6: Load-time curve for the stiffness measurement cycle 68
Figure 6-7: Force-displacement curve of the AFM probe with clutches disengaged 69
Figure 6-8: Force-displacement curve of the AFM probe with clutches engaged 70
Figure 7-1 (a) Dip-pen nanolithography and (b) Diagram of drop-on-demand printing 73
Figure 7-2: Schematic view of the in-plane AFM system used for TERS 75

1. Introduction

1.1 Motivation

Atomic Force Microscopy (AFM) has become an important tool for a large variety of applications since its invention by Binning and Rohrer in the early 1980's, shortly after their invention of the Scanning Tunneling Microscope, for which they received the Nobel Prize in 1986.

AFM can achieve true atomic resolution, and its unique ability to directly probe the surface of a sample and evaluate dimensions in 3D makes it the microscope of choice for a number of applications. Furthermore it has the advantage, compared to Scanning Electron Microscopy, that basically any sample can be scanned, as long as the surface is somewhat solid. Samples can be conductive or non-conductive and placed in basically any environment, from ambient conditions to ultra high vacuum.

While AFM was first used as an imaging tool only, it has proven to be valuable as a tool for far broader applications. Manipulation on a very small scale (sub-micron range) is difficult because there are no dedicated tools for handling available. In recent years, the AFM's use has been extended to various nano/micro-manipulation applications. It can measure and apply a variety of forces and is used to cut, push, pull, and indent nano-scale specimens.

Early on after the invention of the AFM it has been recognized as a powerful tool for biological applications. Conventional microscopy is limited in its application and requires pretreatment of the sample. The AFM, on the other hand, is capable of imaging samples under liquid, making the *in vivo* measurement of biological specimens possible, which is important if the sample has to be kept alive.

Despite its success as a manipulation tool, the basic outline of the system does not reflect other biological measurements than simple imaging. In fact, the design has changed little over the last 20 years. This brings about a number of shortcomings of current AFMs.

Major drawbacks of commercially available AFM are the slow imaging speed as well as the limited scanning area [1]. Tip manufacturing remains difficult and the repeatability of producing tips with uniform shape, which is critical for high-quality imaging, is difficult to achieve. Silicon cantilevers with high Young's modulus and very sharp tips are not optimal for scanning soft biological samples. In addition, the overall architecture of the system, with a cantilever as the transducer for converting force into motion and a laser for measuring the displacement, makes functional integration for other applications than imaging difficult and results in cumbersome yet fragile devices. And the stiffness of the cantilever, which converts the tip´s movement over the sample into a measurable deflection, has to match the hardness of the surface because the deflection of the cantilever should be significantly larger than the intrusion of the tip into the sample. In the current AFM practice, adjustment of the stiffness of the probe to different surface hardness values can only be accomplished by manually changing the probe. This, however, would imply a change of probes in the middle of a measurement and therefore would result in a positional inaccuracy, if the sample has a varying hardness, as it is often the case with biological applications.

The research described in this thesis explains how the shortcomings of current AFM probes with respect to speed, versatility, functional integration, fabrication, and tip have been addressed by redesigning the device with a systems design approach. An in-plane AFM probe is conceived which is specifically tailored to the needs of biological applications. It features a variable stiffness which adopts itself to the changing surface hardness of the sample. Actuation in the z-direction and sensing can easily be integrated onto the coplanar MEMS structure. A carbon nanotube (CNT) can be easily assembled and is used as a high-aspect-ratio tip. The inherent capability of the in-plane AFM probe for building a massively parallel array is an important feature of the new design with a great impact on the speed of the AFM scanning process.

1.2 Device Description

For the integration of the components into the proposed MEMS device, the conventional cantilever-type design of AFM probes has been abandoned in favor of an in-plane design. The in-plane design has a decisive advantage over the conventional cantilever-type design in that it makes the fabrication of the integrated system including sensor, actuator and tip easier and it facilitates arrays of multiple AFM probes.

Figure 1-1 shows the design of the entire device. In order to obtain the surface image of a sample, the tip is brought in contact with the surface. As the probe scans the surface, the tip moves up and down according to the surface topography. The amount of displacement is measured by the capacitive sensor whose output signal is fed back to the comb drive actuator. Based on the closed loop control, the actuator moves the whole system in the vertical direction to maintain a constant force between the tip and the sample. By applying a voltage between the plates of two electrostatic actuators, two additional beams can be attached to the main compliant structure, thus increasing the overall stiffness of the system.

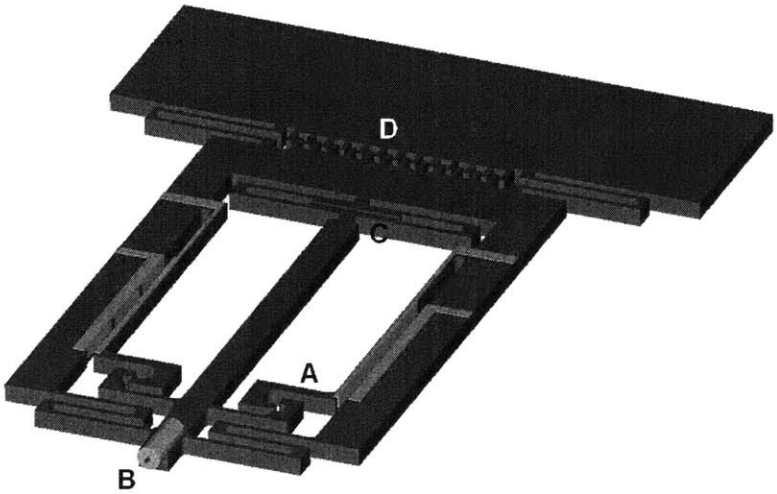

Figure 1-1: Device design (A Electrostatic clutch, B High-aspect-ratio carbon nanotube tip, C Capacitive sensor, D Comb drive actuator).

The device is surface micromachined with the CNT tip to be assembled afterwards. As the structural material, an epoxy-based negative tone photoresist (SU-8) is used. Its low Young's modulus is favorable for achieving a low stiffness device, which is required for biological applications. The metal for the actuators and the sensor as well as for the electrical connections can easily be deposited via e-beam evaporation.

1.3 Competing Solutions

Research has been done to increase the speed of AFM by integrating actuators and sensors in the cantilever [2], by building arrays of multiple cantilevers [3], and by improving the individual parts of the entire AFM [4]. These approaches, however, are mere improvements of current devices. This lack of complete redesign results in devices which are difficult to manufacture and it does not address the special requirements of biological applications, such as multiple stiffness and low-pressure contact. It does not improve the capabilities of the AFM with regard to the manipulation of soft bio-samples and continues to harbor the problems associated with sharpened conical tips common in commercially available AFM probes.

An AFM probe where tip and cantilever lie in one geometric plane which is orthogonal to the sample plane has already been described by [5]. But in contrast to our design the cantilever is vibrated laterally near its resonance frequency and operated in non-contact mode. Interaction forces between sample and cantilever cause changes in the amplitude of this vibration from which the topography of the sample can be deduced. This arrangement prevents damaging the sample but limits the resolvable aspect ratio of objects and makes it impossible to use the AFM as a manipulator. Another AFM with in-plane design has been introduced here [6]. It uses a laterally oscillating beam with a somewhat stationary tip at the end. The system has a very high stiffness which makes it possible to measure high force gradients. Both systems are not optimal for biological applications, which require very low stiffness probes, make system integration impossible, lack manufacturability and prohibit the use as a micro-manipulator.

The use of a carbon nanotube (CNT) as a tip addresses many shortcomings of current AFM tips. AFM probes with CNT tips are already commercially available. However, the present method of mechanically attaching the CNT to the acrylic adhesive coated tip is laborious and depends heavily on the skills of the operator. It also lacks accuracy of alignment and repeatability, which are critical for nano-scale imaging.

1.4 Purpose and Organization of the Document

The purpose of this thesis is to redesign the AFM probe in order to address the shortcomings of current systems with regard to the functional requirements of biological

applications. A variety of applications is studied from which specific requirements are deduced. These are then used to identify design parameters which meet the requirements. A process flow is conceived to manufacture a device for the proof of concept of the switchable stiffness AFM probe.

The document is organized to follow the various design stages, explain the reasoning of how the required applications drive the design parameters, and summarize the manufacturing process. The first chapter provides the necessary background of the current AFM practice and various applications to identify shortcomings of commercially available systems and establish requirements for the design of a new device. Chapter two explains the design process of mapping functional requirements and design parameters and choosing critical parameters such as the overall device stiffness. The new design is described in detail in chapter three, which also includes calculations for the optimal device stiffness for samples with varying hardness. In chapter four the process flow is laid out and manufacturing results are provided. Chapter five shows results from testing the stiffness of the AFM probe and performance of the switchable stiffness. The last chapter includes a discussion of the results, concluding remarks, and suggestions for future work.

2. BACKGROUND

2.1 Current AFM Practice

For the measurement, an AFM probe consisting of a horizontal cantilever beam with an integrated single crystal silicon tip at its end is scanned over a surface (Figure 2-1). As the tip is dragged across the surface of the sample, it follows the slope of the surface, causing the cantilever to bend. The vertical movement of the cantilever is recorded to create a digital image of the sample.

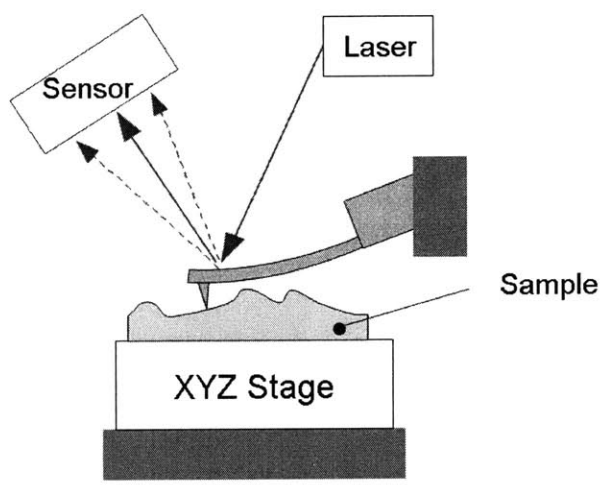

Figure 2-1: Functional overview of a standard AFM system.

Usually a laser beam is reflected off the back of the cantilever and onto a photo sensitive diode. Bending of the cantilever causes the reflected laser beam to expose different areas of the diode, which can be detected with a very high accuracy, resulting in a resolution comparable to that of laser interferometry. This bending can directly be related to the force

acting between tip and sample, as the stiffness of the cantilever is known, according to Hook's Law:

$$\Delta z = \frac{\Delta F}{k} \qquad (2\text{-}1)$$

where z is the vertical position of the tip, F the interaction force between tip and sample, and k the stiffness of the cantilever.

Via closed feedback loop the AFM system not only measures the interaction force, but also regulates this force. In order to hold the interaction force constant, either the sample or the cantilever has to be vertically moved, according to the results of the feedback circuit. This is usually done with a piezo-tube scanner, which provides the necessary resolution and accuracy. Because of this force regulation, the interaction force can be kept very low, in the range of pico-Newton, which is crucial for biological applications. The movement in z-direction required to keep the force constant then represents the topological data of the sample.

There are different operating modes for the AFM. In contact mode, the tip is in physical contact with the sample and simply dragged across the surface. In non-contact mode, the tip-sample distance is at least one nanometer. This mode can be used to measure electric or magnetic properties, like conductivity and charge distribution. In addition, the cantilever can be driven in or near resonance, and frequency or phase shifts due to interaction forces instead of cantilever bending are measured. This allows for the detection of very low forces. In tapping mode the cantilever is oscillated in a way that only intermittent contact with the sample is made. Because the energy transferred from the tip to the sample is much lower than in contact mode, it allows for gentle handling of the specimen, while still enabling to penetrate water layers covering the sample, which would falsify the measurement in pure non-contact mode.

As we will see later, only contact mode is of interest for us, as it is necessary in order to manipulate the sample like membrane penetration.

2.2 AFM Applications

In addition to imaging the topography of a sample with resolutions up to atomic scale, interaction forces like adhesion and friction between the tip of the probe and the sample can

be recorded. Thermal imaging has been shown as well [7]. In conjunction with electrically conducting probes, the AFM can be used for electric force microscopy [8], scanning capacitance microscopy [9], and scanning potentiometry [10], enabling the local measurement of electrostatic forces, charge distribution, voltage drops, capacitance and resistance. By applying a larger force on the sample, its viscoelastic properties can be obtained. It was even used for fracture analysis to measure mechanical properties of nanoscale structures [11].

In addition to measuring various parameters and properties, the AFM has been proven to be useful as a manipulation tool as well. It can be used to push, pull, cut and indent. Scratching of the sample, deposition of particles and of thin layers of organic material (nano-lithography) [12] are other applications.

2.2.1 Biological Applications

Especially biological applications benefits from the ease of use of the AFM. Transmission Electron Microscopy requires cell dehydration, coloring with dyes in order to increase contrast and to highlight internal structures, fixation, and cutting of the sample into thin slices (~ 100nm) [13]. The Scanning Tunneling Microscope is capable of sampling under liquid but only with decreased resolution and tip insulation is required. Compared to this, the AFM is the microscope of choice, as it is the only tool which offers direct surface probing and evaluation of dimensions in 3D. The capability to do this *in vivo* gives a more realistic picture of specimen in their natural environment and has the advantage that samples can be kept alive [14].

Particularly in bio-applications the dual use of the AFM as microscope and manipulator is widely popular. The micromanipulation is mostly used for measuring forces involved in rupturing a single receptor-ligand bond, extending a single molecule like DNA or titin, determining the elastic properties of cells, or deforming a subcellular structure like a neutrophil microvillus [15]. The forces involved are mostly at a pico-Newton level. Measuring or imposing these forces are crucial for understanding of molecular and cellular functioning mechanisms. For this purpose, various techniques have been developed such as optical tweezers, micropipette aspiration technique, magnetic and surface force apparatus.

The AFM proves to be superior to these methods in terms of versatility and ease of use. It can be used to measure adhesive forces between the probe tip and the sample surface and interaction forces between many specific molecular pairs such as avidin-biotin or ligand-receptors were quantitatively measured at the single molecular level [16]. Cell adhesion is of fundamental importance to many biological processes including cellular migration, differentiation, and growth regulation. An example for observation of biological processes on a molecular scale is the enzymatic degradation of DNA [17]. In order to overcome thermal motion and softness of the sample which limit the quality of the measurements, the sample can be cooled down to cryogenic temperatures [18].

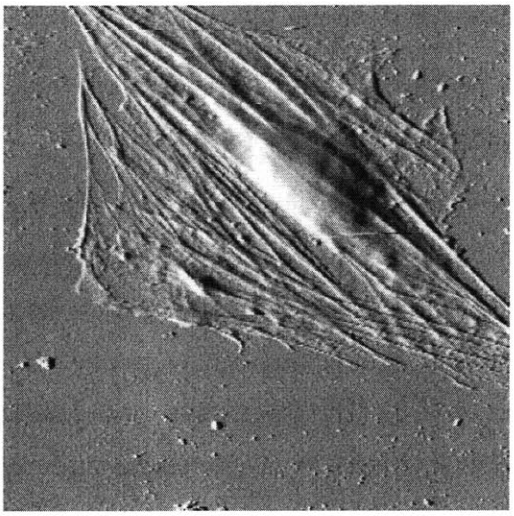

Figure 2-2: Live osteoblast (bone cell) imaged in contact mode under liquid [19].

2.2.2 Special Requirements of Biological Samples

Biological samples have their own very specific requirements. Biological samples are rather soft, which leads to the AFM tip indenting the specimen and causing elastic deformation. As a result, the obtained force curve is flatter and the cantilever deflection smaller compared to sampling a perfectly stiff sample. The resolution is limited by this elastic indentation of the tip into the sample, which is a function of tip shape, probe stiffness, and Young's Modulus of the sample.

The nanoindentation can be useful for measuring the local elasticity of specimens, but in order to maximize resolution, minimize surface erosion and sample damage, the indentation should be kept as small as possible.

One method for achieving this is to increase the hardness of the sample, either chemically or by cooling it. However, this will alter the scanning results and is impossible if in-situ imaging is required. It is therefore crucial to minimize the stiffness of the AFM probe. To a limited extend, one can compensate for the indentation of the probe tip into the sample afterwards. In order to do this, a force-versus-distance curve of a hard sample is obtained first, and by comparing this to the measurements with the soft sample, the indentation can be factored out [20].

Taking the low Young's modulus of living cells into consideration, which is usually around 1-100 kPa, the applied force should be in the range of a few pN with conventional cantilever-style AFM probes with sharp tips [20].

A quantitative model for the effect of indentation on resolution and the relationship between probe stiffness and indentation is given in section 3.3.

Another difficulty for imaging of biological samples like living cells is posed by their varying hardness (Figure 2-3). Cells do not have a homogeneous structure, their hardness depends on the shape of the cytoskeleton – harder areas on the cell result mainly from the concentration of actin filaments. Various studies have revealed that the elastic properties of a single cell vary by a factor of 10-20 [21]. This causes varying indentation of the tip over the sample surface and therefore results in measurement and resolution inaccuracies. To circumvent this, the proposed in-plane design of the AFM probe has a switchable stiffness, as explained in more detail in section 3.2.

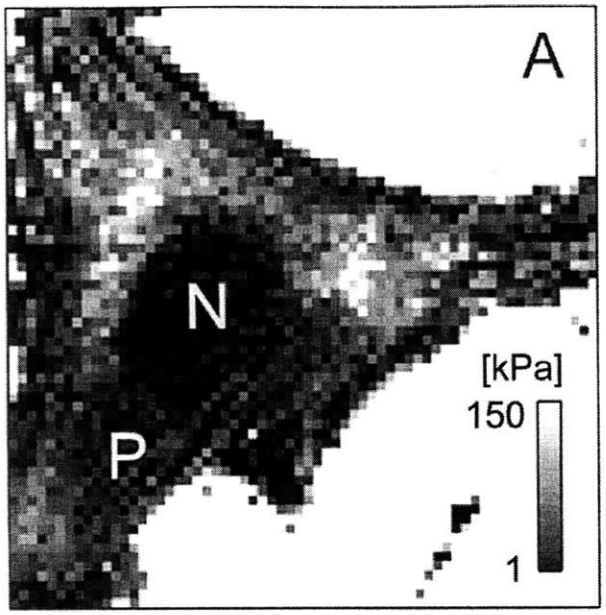

Figure 2-3: Elasticity image of a living fibroblast (NIH3T3) obtained in force mapping mode [22].

2.3 Drawbacks of Conventional AFM

Despite the number of different applications in which the AFM has been proven to be useful, there are some drawbacks of current AFMs.

Because of the limited travel of the cantilever, usually in the range of a few up to 20 micrometer, the surface has to be flat. The AFM has a small scanning area due to the piezotube scanner, which is widely used to drive the cantilever. And, compared to other microscopes, its scanning speed is very low – minutes for a sample size of 100μm x 100μm, while the size of the whole system, consisting of cantilever, piezo-scanner, xyz-stage, and laser sensor, makes the building of arrays impossible. Another issue is the manufacturing of the cantilever and tip. While the cantilever itself does not pose a big challenge, the tip adds another dimension as it sticks out of plane.

A major disadvantage which has not yet been addressed is that the spring constant of the cantilever, which determines the stiffness of the probe, has to match the hardness of the surface in order to optimize resolution, image quality, and tip-sample interaction. Especially for biological applications, where soft samples have to be scanned, an AFM probe with a well-matching, low stiffness is required to prevent surface deformation during scanning.

In the current AFM practice, adjustment of the stiffness of the probe to different surface hardness values can only be accomplished by manually changing the probe. If, however, the surface has an inhomogeneous hardness, as it is seen in biological samples, this would imply a change of the probe in the middle of a measurement and, as a consequence, a loss of positional accuracy of the tip location. Currently the only alternative is to select one stiffness value upfront, which always leads to suboptimal matching of the cantilever deflection to sample indentation.

3. Design Process

3.1 Functional Requirements and Mapping to Design Parameters

The functional requirements of the AFM probe which drive the decisions for the design parameters are deduced from three applications. First of all, the probe will be used as an imaging device. Second, it has to serve as a multi-functional micro-manipulator. And third, it should be tailored specifically to the needs of biological applications. The detailed requirements are shown on the top layer of Figure 3-1, while the bottom layer shows the corresponding Design Parameters.

Requirements for a successful imaging device are high speed and good resolution. The former is met by integrating the actuation in the device and by facilitating the formation of arrays. The latter is ensured by the high-aspect-ratio tip, including the use of a carbon nanotube. In order to provide a versatile manipulation tool, the design of the probe should offer the possibility of handling different types of energy (deliver thermal and electrical energy, measure electrical potential) and enable mechanical handling of the sample. Therefore the design should have room for connections for various energy domains and the tip has to be able to deliver the energy to the sample. In addition to this, biological applications require the probe to work under liquid, scan soft samples and handle samples with varying hardness. The proposed design addresses these issues by providing a very low, variable stiffness and a CNT as the tip.

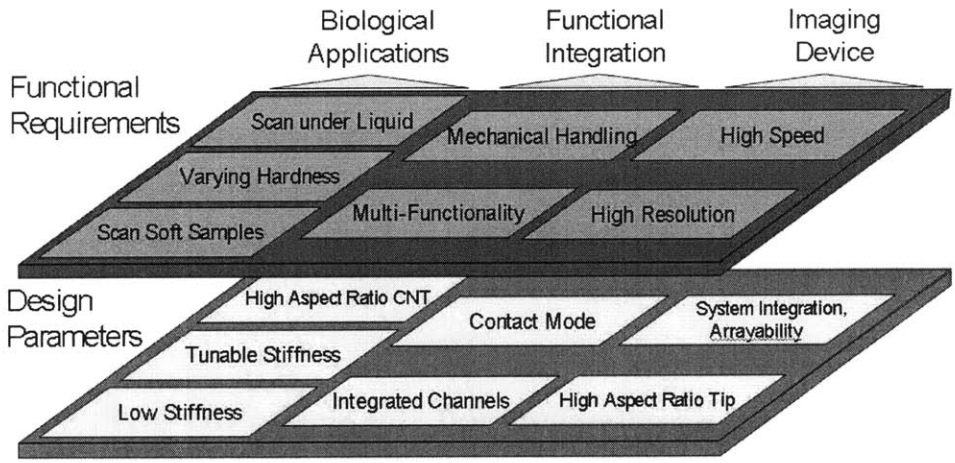

Figure 3-1: Functional requirements (top layer) and the corresponding design parameters (bottom layer).

3.2 Realization of the Switchable Stiffness

First of all, the concept of changing the stiffness has to be chosen because it determines the basic outline of the device. A variety of possible designs have been evaluated including the following:

- Variation of the geometry
  - Preloading of a spring: This technique is frequently used in macro-applications like bicycle suspensions, for example. Squeezing the spring increases the amount of initial force needed to activate it.
  - Variation of the length of a beam: The spring constant of a beam depends on the length of the beam. Since the spring constant varies with the length to the third power, a high ratio of stiffness change can be achieved with this method.
  - Alternating the number of involved springs: With a slight variation this method has been implemented.
- Use of a compressible fluid: Air suspension in some automobiles makes use of this principle. By varying the pressure in a confined compartment, the stiffness can be changed.
- Use of actuators to provide a force opposing the tip movement, effectively changing the stiffness of the probe as seen by the sample.

After reviewing these different concepts a set of characteristics were chosen and on this basis the concepts were evaluated. The result is summarized in Table 3-1.

Table 3-1: Comparison of different design alternatives.

	Preloading of spring	Varying beam length	Change number of springs/beams	Compressible fluid	Actuator
compact	-	+	o	-	+
low stiffness	+	+	o	o	+
robust	-	+	+	--	o
easy to fabricate	--	-	+	--	--
highly dynamical	+	+	+	o	o
connectivity	-	-	+	-	o
stiffness range	--	-	++	o	++

In the end, we are pursuing a continuously variable stiffness, which can be achieved by means of an actuator. As a first step a design was chosen which provides two different stiffness values, which can be achieved by de- or attaching additional beams. We chose to achieve tunable stiffness by alternating the number of beams which suspend the tip. This method provides a wide range of stiffness with one device. It is robust and easy to fabricate.

Various alternatives of switching on/off multiple flexures to the main structure have been investigated and an electrostatically actuated clutch is designed. Electrostatic actuators have been chosen to operate the clutches because of their simplicity, low power consumption, and manufacturability. The two parts of the clutch provide a form fit in order to prevent a relative movement (slip) between the two sides of the clutch in the vertical direction when it is closed. The following figures show three steps of design iterations.

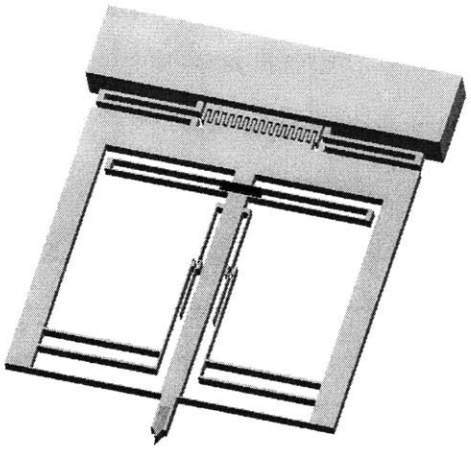

Figure 3-2: Additional beams can be attached with the help of electrostatic actuators ("clutches").

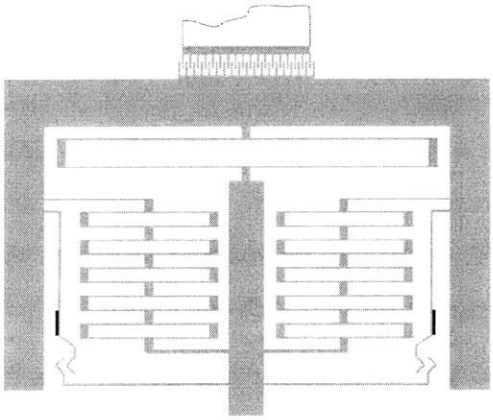

Figure 3-3: The "clutches" which attach additional beams are moved to the outside of the system in order to reduce the mass of the moving part.

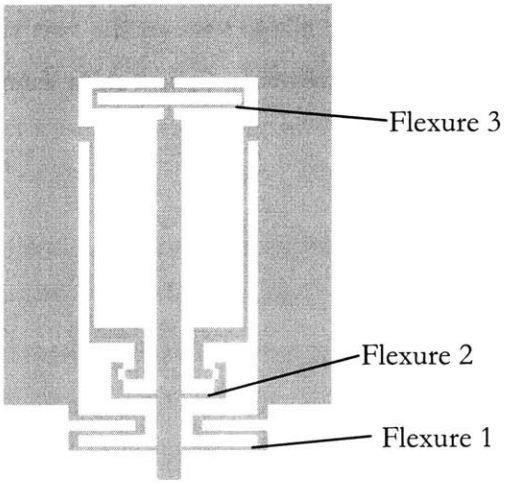

Figure 3-4: Plain structure of the AFM probe without sensors, actuators, tip.

For the integration of the components into the proposed MEMS device shown in Figure 3-4, the conventional cantilever-type design of AFM probes has been abandoned in favor of an in-plane design. The in-plane design has a decisive advantage over the conventional cantilever-type design in that it makes the fabrication of the integrated system including sensor, actuator and tip easier and it facilitates arrays of multiple AFM probes.

Driving factors for the final design of the entire structure are low stiffness in the z-direction, minimized out of plane movement as well as integrated actuators and sensors. The probe beam is suspended by flexures, enabling it to follow the topography of the sample. The box-like structure (flexure 3) at the top and the folded beam structure at the tip are designed to meet the specifications of stiffness and out-of-plane restraint (Figure 3-4).

3.3 Determining Optimal Probe Stiffness

A variety of requirements with respect to the stiffness of the probe arise from the nature of the applications and the performance targets. These requirements set limitations for both the lower and upper bounds of the stiffness. This section provides the modeling of stiffness limitations and background information for choosing the optimal stiffness. As it will be shown, the indentation depth of the tip into the sample, which determines the resolution of the AFM probe, will be the main factor in choosing a lower bound stiffness.

3.3.1 Lower limit for the probe stiffness – reasons for choosing a high stiffness

1. The resonant frequency f_0 of the device must be high enough so that it is not limiting the speed of scanning the surface topography (i.e. the eigenfrequency should be significantly higher than the desired detection bandwidth). This requires a resonant frequency in the range of 1 kHz or higher.

   The resonant frequency is a function of the overall stiffness k, which must be high enough to satisfy this requirement. The following first-order model provides a rough estimation.

$$f_0 = \frac{1}{2\pi}\sqrt{\frac{k}{m}} \qquad (3\text{-}1)$$

$$k \succ m(2\pi f_0)^2 \qquad (3\text{-}2)$$

A required resonant frequency of 1 kHz and a mass of the moving part of the probe of 0.3 μg lead to

$$k_{low,1} \succ 0.01 N/m . \qquad (3\text{-}3)$$

2. The stiffness should be high enough to minimize "jump to contact", a tip instability, which occurs during the approach of the tip to the sample when the attracting forces pull the tip into the sample. This can possibly damage a soft specimen.

   Figure 3-5 shows the interaction force **F** as a function of tip-sample distance **D** and a line with the slope of the probe stiffness **k**. As the tip comes closer to the sample it will become unstable at point B and jump to B'. In order to prevent this, the tip-sample stiffness of the probe has to be greater than the maximum of the tip-sample potential V_{ts}:

$$k \succ \max(-\frac{\partial^2 V_{ts}}{\partial D^2}) . \qquad (3\text{-}4)$$

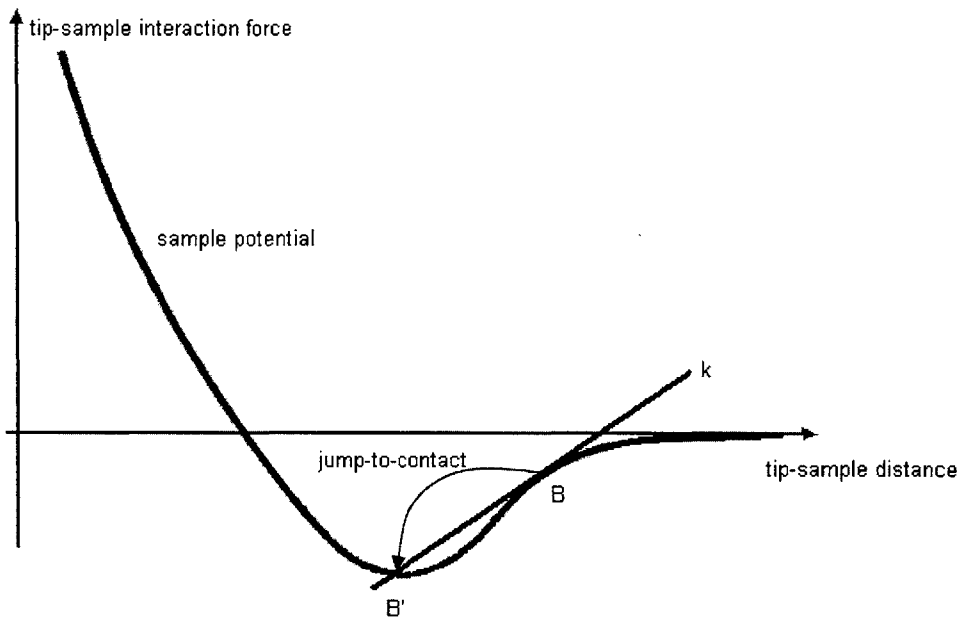

Figure 3-5: Interaction force F as the tip approaches the sample. The slope of the straight line represents the stiffness k of the AFM probe. At the tip-sample distance B the tip will jump to distance B' (red arrow)

The tip-sample potential describes the interaction between tip and sample and it consists of a variety of forces. Their contributions can be classified by their range and strength. In vacuum, there are electrostatic and magnetic forces dominating at longer ranges, while at closer distances of several tens of angstrom van-der-Waals forces are prevalent. At a very short range chemical forces play a role as well. In ambient conditions, capillary forces formed by adhesion layers on tip and sample can be present as well. During contact, elastic repulsion forces dominate, which can be modeled with the Hertz approximation [23].

To model the "jump to contact", the van-der-Waals forces, which are caused by fluctuations in the electric dipole moment of atoms and their mutual polarization, will be estimated. All the other forces can be neglected, because van-der-Waals interactions are predominant at the tip-sample distance of interest.

The van-der-Waals potential **V** for a flat surface (the tip of the carbon nanotube) and the curved surface of a cell membrane is calculated according to [24]:

$$V = \frac{A r_{cell}}{6D} \qquad (3\text{-}5)$$

where **A** is the Hamaker constant for the interaction of the two materials, r_{cell} the radius of local slope of the sample surface, and **D** the tip-sample distance. **A** can be calculated from the individual Hamaker constants of the tip and sample material A_{cnt} and A_{cell}:

$$A = \sqrt{A_{cnt} A_{cell}} \qquad (3\text{-}6)$$

Equations (3-5) and (3-6) can be put into (3-4) and solving the differential in the resulting equation leads to

$$k \succ \max\left(-\frac{A r_{cell}}{3D^3} \right) \qquad (3\text{-}7)$$

The critical distance D_{jtc} where "jump to contact" will most likely occur is calculated according to [25] to be in the range of 0.2-2.1 nm. Using this and A_{cnt}=50e-20 J, A_{cell}=3e-21 J, and r_{cell}=2 nm, we can solve Equation (3-7) and calculate a lower limit for the stiffness

$$k_{low,2} \succ 0.003 N/m. \quad (3\text{-}8)$$

Taking only the van-der-Waals interactions into consideration, this approximation is too low, and in reality the stiffness may not be high enough in order to completely prevent "jump to contact". However, the calculation provides the order of magnitude for a lower limit of the probe stiffness.

3.3.2 Upper limit for the probe stiffness – reasons to choose a low stiffness

1. The resonant frequency of the probe must be lower than the bandwidth of the AFM electronics, which is typically 500 kHz.
   Using equation (3-2), an upper limit for **k** can be estimated

$$k_{high,1} \prec 3000 N/m. \quad (3\text{-}9)$$

2. In order to prevent damaging the sample, the pressure applied by the tip has to be lower than the ultimate strength of the material of the sample. The following calculation provides an approximation for the contact pressure, which is a function of the probe stiffness.

   Elastic deformation at the tip-sample interaction can be calculated with a Hertz analysis [26]. In order to simplify the calculations, the following assumptions are made:

   a) Tip and sample materials are isotropic.
   b) The geometry of the contact area can be described by a sphere with a given radius of curvature r_{cnt} (for the tip) and r_{cell} (for the sample).
   c) Deformations are small with respect to r_{cnt} and r_{cell}.

   Figure 3-6 shows a model of the tip and sample in contact. The depth of indentation **h** depends on the curvature of the tip and sample. The tip of the CNT is here assumed to almost flat, as it can be seen in Figure 3-7. The curvature of the sample depends on the local position of interest. A rather small radius for r_{cell} is used in order to estimate the worst case scenario.

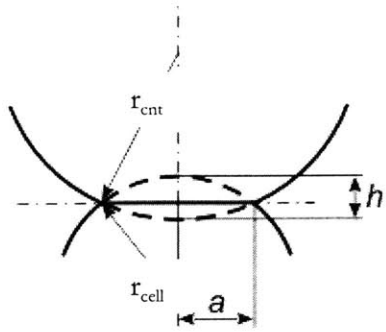

Figure 3-6: Hertz model of the tip and sample indentation depth h.

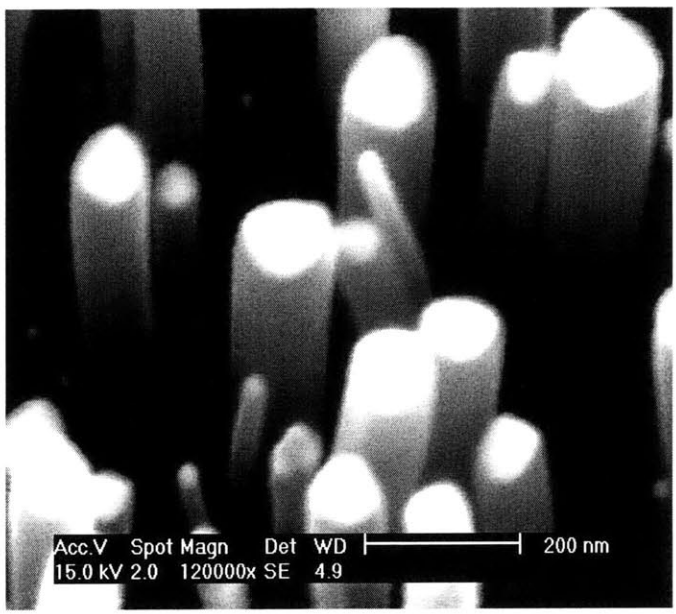

Figure 3-7: SEM picture of the tip of carbon nanotubes.

The effective stiffness (Young's modulus) of the pair of materials is given by

$$\frac{1}{K} = \frac{3}{4}\left(\frac{1-\nu_{cnt}^{2}}{E_{cnt}} + \frac{1-\nu_{cell}^{2}}{E_{cell}}\right) \qquad (3\text{-}10)$$

where E_{cnt} and E_{cell} are the Young's moduli of the CNT tip and sample material (living cell) and ν the corresponding Poisson ratios.

For small indentation depth **h** the following relationship with the radius of contact area a derived from Figure 3-6 is valid

$$h = \frac{a^2}{R} \tag{3-11}$$

using the following relationship for simplification

$$\frac{1}{R} = \frac{1}{r_{cnt}} + \frac{1}{r_{cell}} \tag{3-12}$$

The solution is then

$$F = \frac{Ka^3}{R} = Kh^{\frac{3}{2}}R^{\frac{1}{2}} \tag{3-13}$$

or

$$P = \frac{F}{\pi a^2} = \frac{1}{\pi}\sqrt[3]{\frac{FK^2}{R^2}} \tag{3-14}$$

where **F** denotes the applied force and **P** the applied pressure. Equation (3-14) can be solved for **F**

$$F \prec P\pi a^2 = \frac{R^2(P\pi)^3}{K^2} \tag{3-15}$$

Damaging or puncture of a cell can occur when the shear stress from the applied tip-load exceeds the shear strength of the cell membrane. Using a living cell as a sample, this will occur at a pressure of around 100 MPa. This maximum pressure and the following values are used in the calculation.

$E_{cnt} = 1200$ GPa	$E_{cell} = 1\ldots100$ kPa
$\nu_{cnt} = 0.2$	$\nu_{cell} = 0.2\ldots0.5$
$r_{cnt} = 500$ nm	$r_{cell} = 2$ nm

Together with Equation (3-115) a maximum value for the applied force is calculated, which cannot be exceeded if sample damage is to be minimized

$$F_{max,damage} = 64.0\ \mu N. \tag{3-16}$$

From this and the resolution of the sensor which detects the tip movement, a maximum value for the stiffness of the probe can be calculated. A tip movement smaller than the resolution of the sensor cannot be detected and therefore the height of the sample will not be adjusted via feedback. Thus, a tip movement of the order of the resolution of the sensor d_{res} should not produce a force exceeding $F_{max,damage}$. Tip movement and force are correlated by the probe stiffness according to Equation (3-16). If the stiffness is too high, a tip displacement smaller than the resolution of the sensor will produce a force which damages the sample, without the feedback loop being able to adjust the force via altering the probe or sample height.
From this an upper limit for the device stiffness can be calculated

$$k = \frac{F_{max,damage}}{d_{res}} \qquad (3\text{-}17)$$

Assuming a simple capacitive sensor with a resolution of 1 nm, this leads to

$$k_{high,2} \prec 640 N/m. \qquad (3\text{-}18)$$

3. The indentation of the tip into the sample limits the resolution, as discussed in section 2.2.2. Here, the minimum characteristic feature size, which can be detected by the AFM probe (e.g. the resolution), is of the order of the deformation of the sample under the applied load of the tip. For all practical purposes, the resolution will not be better than the size of the tip, when biological specimens are sampled. Thus, the indentation should not be bigger than the tip of the probe, as the size of the probe tip provides a natural limit for the resolution. Therefore the indentation h of the tip into the sample should not exceed 100 nm for our device, which is the diameter of the multiwall CNT tip. Equation (3-13) relates force and indentation from which a maximum force of

$$F_{max,resolution} = 20 \text{ pN} \qquad (3\text{-}19)$$

is calculated.

According to Equation (3-13) this leads to a maximum value for the device stiffness of

$$k_{high,3} \prec 0.02 N/m. \qquad (3\text{-}20)$$

The exact indentation depth depends on the exact hardness of the sample at the point of contact and its geometry.

These calculations show that the contact pressure is higher for stiffer samples, because the smaller indentation leads to a smaller area of contact. It should also be noted that the Hertz model provides a rather crude approximation of the geometry of tip and sample interaction. However, a more accurate and complex model is not justified since the assumption about the isotropy of tip and sample material may not be very accurate at this small scale.

3.3.3 Choosing the stiffness

The above calculations show that the device stiffness should fall between

$$k_{low,1} \succ 0.01 N/m$$

and

$$k_{high,3} \prec 0.02 N/m .$$

In order to maximize the resolution of the AFM probe and minimize sample damage, the lower of the two stiffnesses of the switchable probe is chosen to be k_{low} = 0.01 N/m. The higher of the two stiffnesses is chosen according to the application of sampling living cells. As shown in [22], the nuclear portion of a cell is about ten times harder than its surroundings (Figure 3-8), which leads to a probe stiffness of k_{high} = 0.1 N/m.

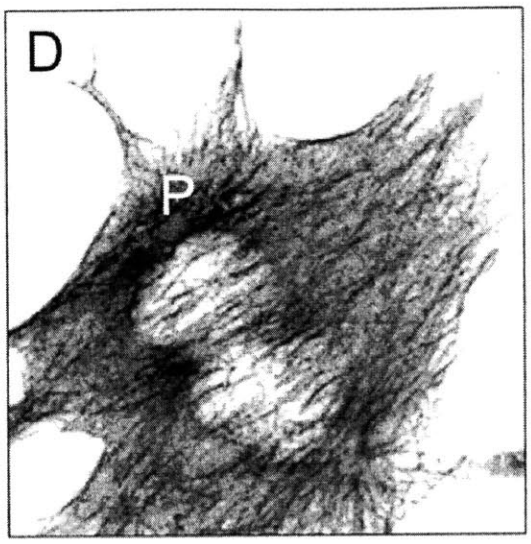

Figure 3-8: AFM image of a living mouse fibroblast [22].

3.4 Tip Design

Since the resolution of the image depends heavily on the tip which is used to probe the sample, tip-sample interaction has been thoroughly investigated. Tip artifacts lead to anomalous images [27, 28, 29] and therefore the tip should be well characterized [30].

Commercially available AFM probe tips consist of Si or Si_3N_4 and possess usually either conical or pyramidal tips. The tip is characterized by the tip radius, the half cone angle (typically 45° for pyramid tips and 10° for conical tips) and the tip height. A small radius is a major contributor to achieve high resolution imaging. The angle of the steepest wall which can be imaged with a specific tip depends on the half-cone angle of the tip unless the tip is tilted with respect to the sample. The height of the tip finally determines the capability of the tip to scan a sample with deep structures.

In current AFM probes the tip is orthogonal to the cantilever. The tip is either indirectly manufactured (holes with the desired shape are etched in a silicon substrate and then filled with the tip material) or directly etched in the tip material [31]. This can be done by plasma etching or KOH etch which selectively attacks specific crystallographic planes of the silicon lattice [32, 33]. A focused ion beam treatment of the tip has been applied to produce tips with high aspect ratio [34]. Etching as a self-sharpening process can deliver tips with radii with less than 5 nm but tips will vary from one to the other even within the same batch. This

means the actual tip geometry is unknown unless a SEM/TEM picture is taken or a sample of known topography (a tip characterizer) is imaged first.

The discovery of carbon nanotubes by Ijima [35] provided new possibilities for AFM tips. With a small diameter and cylindrical high aspect ratio shape, CNT have the right geometry for achieving high quality images. They have a high durability against wear [36] and if wear does occur, the tip diameter does not change because of the vertical sidewalls. They possess a high Young´s modulus and bend elastically to return to original shape. Another plus are good electrical and thermal conductivity. Especially for biological applications the CNT is interesting because imaging soft samples like cells requires somewhat dull tips since the pressure applied by a very sharp tip can be high enough to damage the sample. Because of the described advantages a CNT is the tip of choice for the in-plane AFM.

There are already commercially available AFM probes with CNT tips available. However, the present method of mechanically attaching the CNT to the acrylic adhesive coated tip is laborious and depends heavily on the skills of the operator. The typical assembly operation starts with coating the bottom 1-2 μm section of the silicon tip with an acrylic adhesive and then bringing this tip into contact with the side of a bundle of 5-10 multiwalled carbon nanotubes [37, 38]. Once attached, the nanotube is pulled free from its connections with other nanotubes. Then, these tips are usually inspected in the SEM from two directions to ensure that they are within ± 5 degrees of perpendicularity to the sample, Figure 3-9. Lengths and diameters vary with typical lengths being 500-2000 nm and typical diameter 10-40 nm [39].

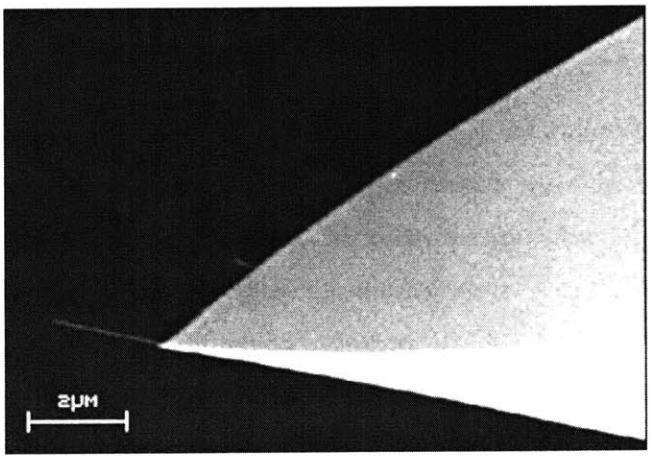

Figure 3-9: CNT as AFM tip [39].

During examination in SEM, if the angle of the CNT tip is not within the prescribed tolerance range, it is very difficult to realign the CNT tip because of bonding with the acryl adhesive. In addition, if the attached CNT is long, which is often the case, it cannot be repositioned, but it has to be shortened by applying bias voltage between the tip and a sputtered Nb surface [37]. Assembled in the above-mentioned way, every AFM probe with CNT tip is different from the other and needs an extensive tuning operation prior to usage.

The other way to attach the carbon nanotube is to grow it directly on the tip [40]. After flattening a conventional silicon tip at its apex by contact AFM imaging and anodizing it in hydrogen fluoride to create nanopores of 50-100 nm diameter along the tip axis, iron catalyst is electrodeposited into the pores from $FeSO_4$ solution and nanotubes are grown by CVD with ethylene and hydrogen. They are usually too long to be used and therefore must be cut. This method is less laborious than the mechanical assembly, but it is difficult to control where exactly the nanotube is grown and therefore, uniformity of the AFM tips is difficult to achieve.

The fact that the single CNT needs to be assembled in the plane of the AFM probe doesn't alleviate the assembly operation compared to the vertical attachment of CNT to the cantilever-type AFM probe. To accomplish the in-plane assembly in a simpler way, the concept of the nanopelleting technique will be utilized. This technique has been invented to make carbon nanotubes assemblable and manufacturable and been disclosed in "Method of Making Packets of Nanostructures" [41].

This high-aspect-ratio tip is made of a 'nanocandle' (Figure 3-10 a), which consists of a single strand carbon nanotube embedded in a high-aspect ratio cylindrical block made out of a polymer. The diameter of the nanocandle can be chosen as convenient and therefore effectively scales up the tip to a size which is large enough to be handled. This novel nanoblock allows a rapid in-plane assembly of the carbon nanotube to the AFM probe for achieving a high lateral resolution.

The in-plane assembly of the high-aspect-ratio nanopellet can be simply accomplished by mechanically pushing it with conventional micro probe tip into a V-groove, Figure 3-10 b.

Once in the groove, it can be axially aligned along the groove and fixed with a drop of epoxy. This mechanical handling means a unique possibility to position the carbon nanotube tip exactly where it should be in the plane of the AFM probe.

The controllability of exposed CNT length with the mechanical positioning allows the manufacture of truly uniform AFM tips, which hasn't been so far possible with the conventional CNT assembly method.

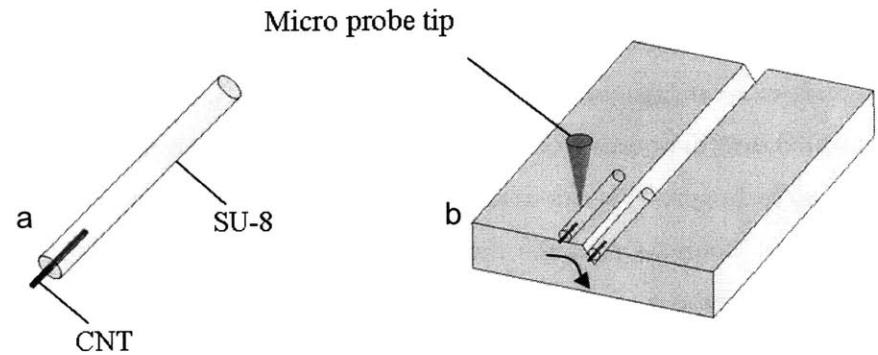

Figure 3-10: Nanopellet with carbon nanotube (a) and its assembly into a V-groove (b).

4. Device Description

4.1 Overview

For the integration of the components into the proposed MEMS device shown in Figure 4-1, the conventional cantilever-type design of AFM probes has been abandoned in favor of an in-plane design. The in-plane design has a decisive advantage over the conventional cantilever-type design in that it makes the fabrication of the integrated system including sensor, actuator and tip easier and it facilitates arrays of multiple AFM probes.

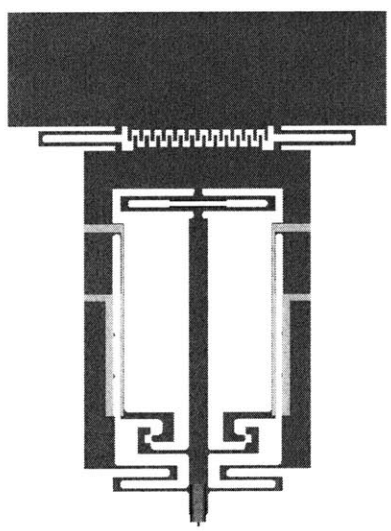

Figure 4-1: CAD model of the in-plane AFM probe.

After investigating various alternatives of switching on/off multiple flexures to the main structure, an electrostatic clutch is designed. Electrostatic actuators have been chosen to operate the clutches because of their simplicity, low power consumption, and manufacturability. The clutches are designed in a way that the actuator is not part of the moving structure. This reduces the weight of the moving part and decreases response time.

In order to prevent contact between the two metal counterparts of the actuator, which would result in a short circuit, small supports are included in the structure. The two parts of the clutch provide a form fit in order to prevent a relative movement (slip) between the two sides of the clutch in the vertical direction when it is closed (Figure 4-2). In order to make sure that the clutches can safely slide in, the inner peg is chamfered and the outer part has rounded edges. Taking a friction coefficient of 0.19 for SU-8 as the structural material into account, a contact angle between the inner and outer part of 79° or less has been calculated as the limit for being able to pull in the clutch.

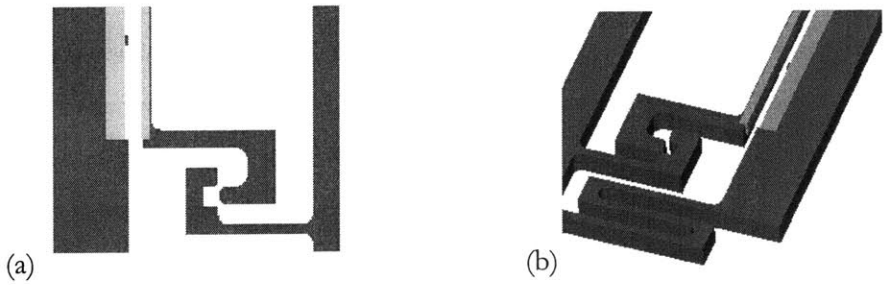

Figure 4-2: Close up view of the clutch (a: top view, b: 3D view).

4.2 Sensor

The displacement of the tip has to be measured in order to obtain the surface image. A capacitive sensor will serve this purpose because it is easy to integrate and can be manufactured in one step with the electrostatic actuators of the clutches. It is also favorable because sub-nanometer resolution can be achieved.

4.3 Final design

Figure 4-3 shows the entire device. In order to obtain the surface image of a sample, the tip is brought in contact with the surface. As the probe scans the surface, the tip moves up and down according to the surface topography. The amount of displacement is measured by the capacitive sensor whose output signal is fed back to the combdrive actuator. Based on the closed control loop, the actuator moves the whole system in the vertical direction to maintain a constant force between the tip and the sample. By applying a voltage to the plates of two electrostatic actuators, two additional beams can be attached to the main compliant structure, thus increasing the overall stiffness of the system.

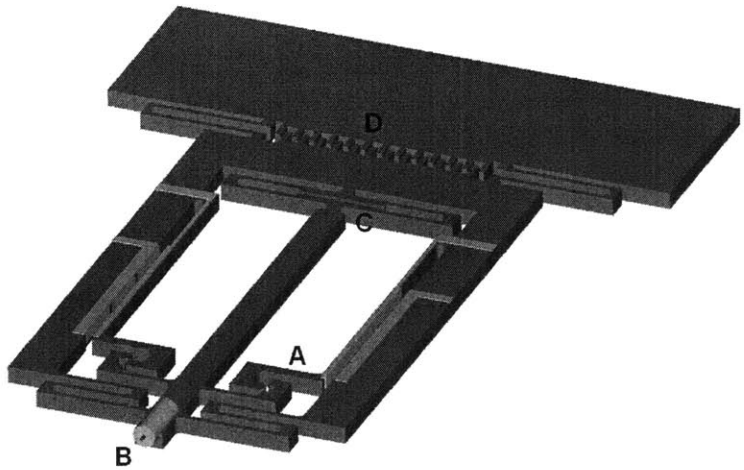

Figure 4-3: Device design (A Electrostatic clutch, B High-aspect-ratio carbon nanotube tip, C Capacitive sensor, D Combdrive actuator).

4.4 Stiffness Model

The stiffness of the entire device has been calculated by approximating the structure with a lumped model of ideal elastic beams (Figures 4-5, 4-6, 4-7). Each flexure of the device is modeled as a combination of individual beams which have zero slope at both ends (Figure 4-4). The rest of the structure is assumed to be rigid.

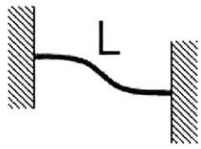

Figure 4-4: Ideal beam with zero slopes at both ends.

The stiffness for one beam with length L, width w and thickness t can be calculated according to

$$k_{beam} = \frac{12EI}{L^3} \tag{4-1}$$

where E is the Young´s modulus and I the area moment of inertia

$$I = \frac{wt^3}{12} \tag{4-2}$$

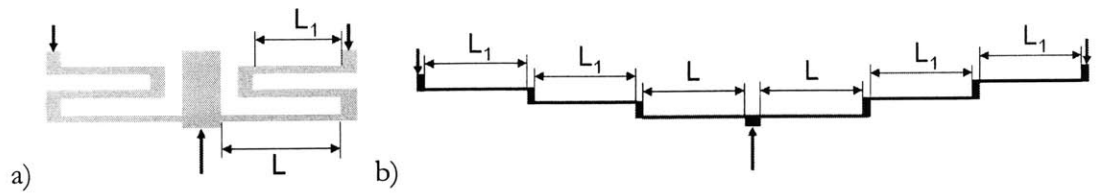

Figure 4-5: Flexure 1 (a) and its lumped model (b).

The stiffness of flexure 1, which is shown in Figure 4-5, can be modeled as

$$k_1 = 2\frac{Ewt_1^3}{L^3 + 2L_1^3} \tag{4-3}$$

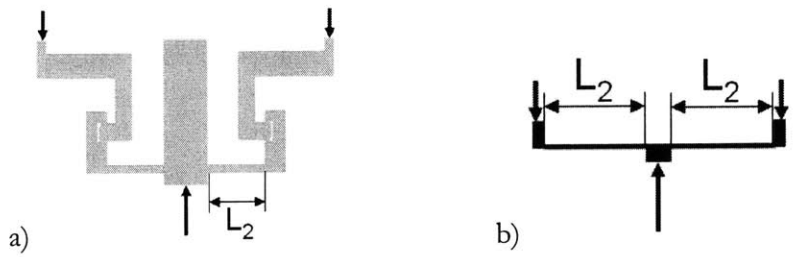

Figure 4-6: Flexure 2 (a) and its lumped model (b).

The stiffness of flexure 2 (Figure 4-6), representing the device with the two clutches engaged, can be modeled as

$$k_2 = 2\frac{Ewt_2^3}{L_2^3} \tag{4-4}$$

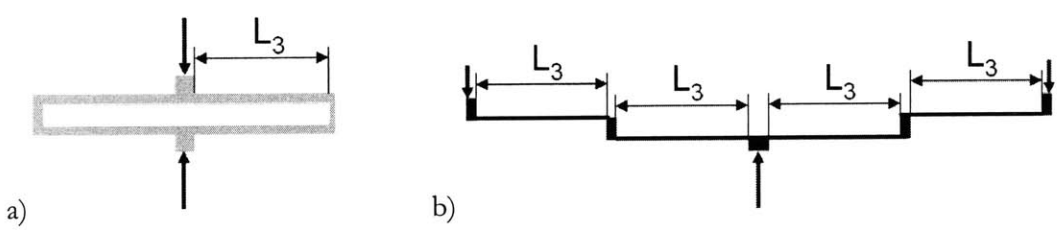

Figure 4-7: Flexure 3 (a) and its lumped model (b).

The stiffness of flexure 3, representing the base of the device (Figure 4-7), is modeled as

$$k_3 = \frac{Ewt_3^3}{L_3^3} \tag{4-5}$$

Target values for the final design are a stiffness of 0.01 N/m in the soft mode (k_1+k_3) and 0.1 N/m in the hard mode with the clutches closed ($k_1+k_2+k_3$). To achieve these values, a beam width of 1-2 μm is necessary and the overall size of the system has to be 500 μm by 650 μm.

The proof-of-concept design, which has been fabricated first, makes use of a low-cost transparency mask whose limited resolution results in a minimum beam width of 14.5 μm. It has a calculated stiffness of 53.7 N/m in soft mode and 122 N/m in high stiffness mode.

The target for the final device is to have a k_{high}/k_{low} ratio of ten, and the tunability can be easily achieved by adjusting the additional beams to the corresponding thickness. The proof-of-concept device achieves a stiffness ratio of approximately two. This is due to the fact that the width of the beam has been increased tenfold, while the length and the thickness of the device are increased less than twofold. By selectively increasing the width of the additional beams which are attached by the means of the clutch, a stiffness ratio of ten could have been achieved, but this would have increased the stiffness of the device in high mode to a value which could not have been measured with the Hysitron nanoindenter (section 6.2).

4.5 Pull-In Voltage of the Clutches

A simplified calculation of the pull-in voltage of the electrostatic actuators has been performed following the method described by Senturia [42]. From the total derivative of the co-energy,

$$W^*_{(V,g)} = \frac{\varepsilon A V^2}{2g} \tag{4-6}$$

the pull-in voltage can be calculated to

$$V_{pi} = \sqrt{\frac{8kg_0^3}{27\varepsilon A}} \tag{4-7}$$

and the gap where pull-in occurs is

$$g_{pi} = \tfrac{2}{3} g_0 \tag{4-8}$$

A is the surface area of the electrostatic plates, V the applied voltage, g the gap between the two plates, ε the electrical permittivity, k the stiffness of the clutches and g_0 the initial gap. It can be seen that the value of the necessary voltage depends on the size of the actuator as well as on the width of the air gap between the plates of the clutch and its stiffness. The

pull-in voltage has also been simulated with the MEMCAD software package and calculated to be around 135 Volts for the large proof of concept design (Figures 4-8, 4-9).

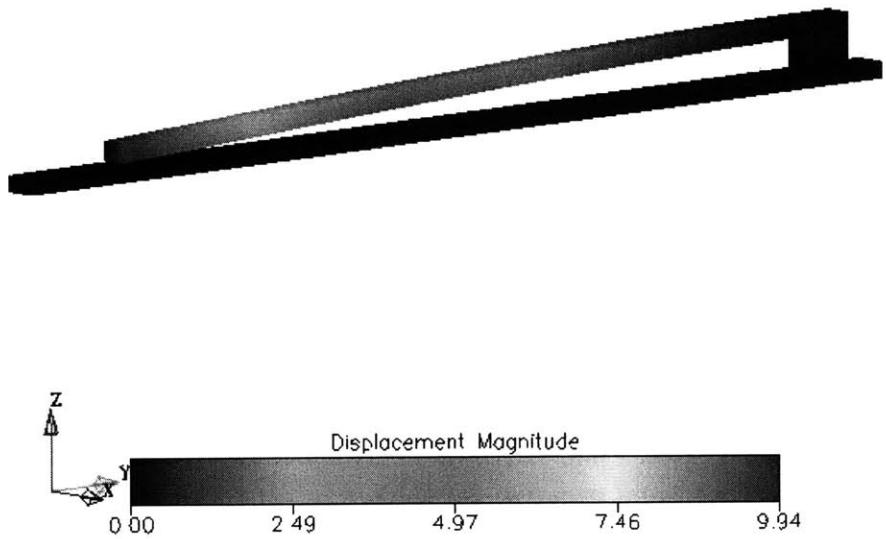

Figure 4-8: 3D-model for the simulation of the pull-in voltage of the electrostatic actuator.

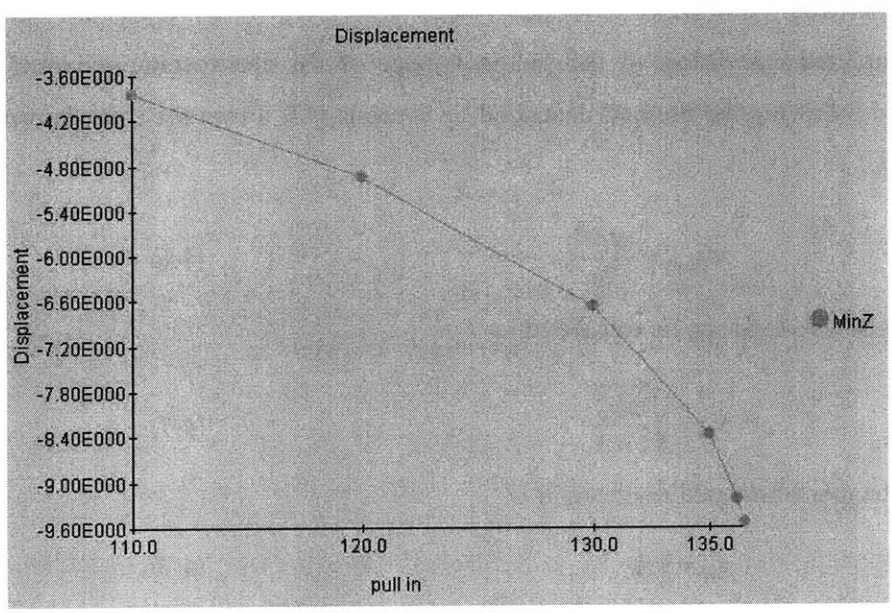

Figure 4-9: MEMCAD result for the pull-in voltage of the electrostatic actuator.

4.6 Dynamic Model and Testing

In order to quantify the anticipated dynamic response of the AFM probe, a Finite Element Analysis is carried out as well as experimental testing on a scaled up macro-model [43].

For the computer analysis a 3D model is generated and the frequency response calculated with the software ANSYS 8.0. The analysis assumes undamped vibrations of harmonic form described by

$$\{u\} = \{\phi\}_i \cos \omega_i t \qquad (4\text{-}9)$$

where $\{\phi\}_i$ is the eigenvector representing the mode shape of the ith natural frequency, ω_i is the ith natural frequency, and t is time.

In addition, a high speed video camera capturing 4200 frames per second is used to record the motion of a scaled-up model. The frequency response of the same model is further analyzed with a sound-wave detection setup. The results are then scaled down according to the ratio of the dimensions of the micro and macro model.

This analysis reveals a natural frequency of 51 kHz in the vertical direction (along the axis of desired tip motion), of 55 kHz in the out-of-plane direction, and of 81 kHz in the horizontal direction.

Figures 4-10 and 4-11 below show the results summary for each device setting, both engaged and disengaged.

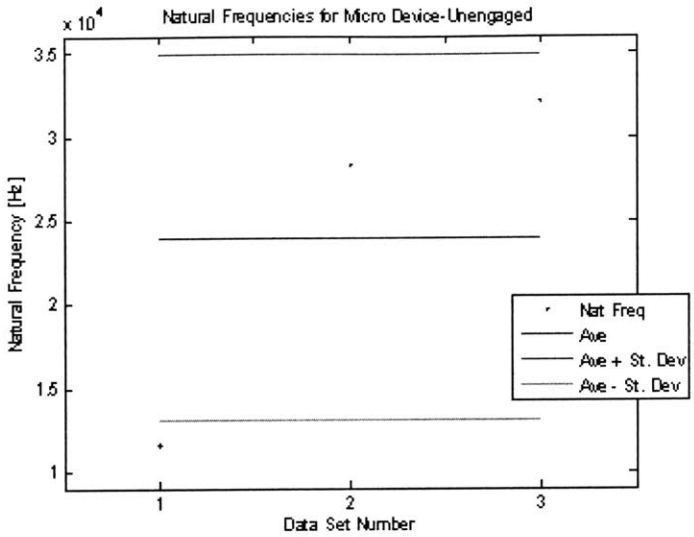

Figure 4-10: Natural frequencies of the device in disengaged mode.

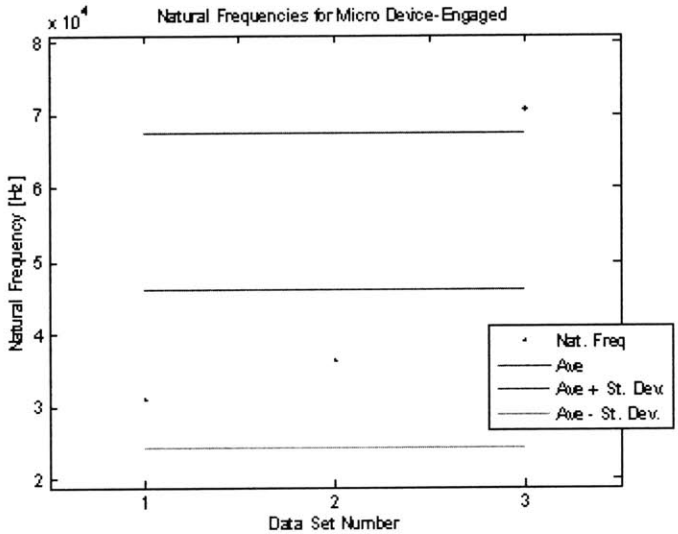

Figure 4-11: Natural frequencies of the device in engaged mode.

5. Manufacturing

5.1 Process Flow Overview

The entire device is surface micromachined with conventional MEMS fabrication processes and the tip will be assembled afterwards. Test grade silicon wafers with a diameter of 100 mm (both n-type and p-type) have been used as the fabrication base. The quality of the wafers is of minor importance since they have merely a supporting function.

As the structural material, SU-8 is used. It is a chemically amplified epoxy-resin negative tone photoresist developed by IBM [44]. SU-8 is available in a variety of types to achieve film thicknesses from less than 1 μm to over 200 μm, making MEMS structures with exceptionally high aspect ratios possible. It has high optical transparency and is sensitive to near UV radiation (350-400nm). Once cured, the SU-8 is highly resistant to solvents, acids, and bases and possesses excellent thermal stability. The good mechanical properties of SU-8 have led to a wide range of applications in the field of MEMS. It has been used to form micromolds [45] and for a variety of microfluidic devices [46]. SU-8 also proved to be successful as the structural basis for a number of MEMS devices [47, 48].

The metal for the actuators as well as for the electrical connections is deposited via e-beam evaporation. The finished device is then released by XeF_2-etching. A process flow can be seen in Figure 5-1.

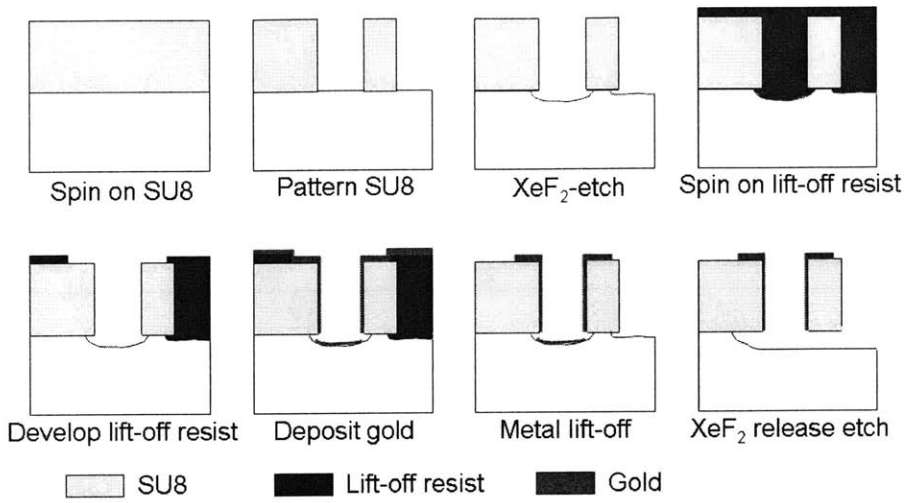

Figure 5-1 : Process flow.

5.2 Mask Design

For all lithography processes used during fabrication, transparency masks are generated firstly and the patterns are subsequently transferred to chrome-glass masks. Before designing the masks, the limitations of the transparency mask making process have to be considered. Since the laser photoplotters used in the mask making process require at least 8 to 10 pixels to form a line, the minimum achievable feature size with this mask is 8-10 μm. Tolerances for small geometric patterns are within about three times the resolution of the plotter, leading to a tolerance of +/-0.5 μm. A measured amount of edge roughness of 1-2 μm has to be expected as well. As a result, the overall size of the device has to be scaled up in order to be fabricatable with transparency masks. Instead of a targeted beam width for the final device of 1.5 μm, the beam width of this scaled-up device becomes 10 μm. This scaled-up device functions as a proof-of-concept model for the switchable stiffness and is used to establish and optimize a reliable fabrication process. Figure 5-2 shows that this design pushes the transparency mask to its limit.

The 4" wafer provides ample space for the batch fabrication of a large number of devices. This makes the simultaneous fabrication of devices with design variations possible, which allows testing and picking the best design after manufacturing. Since the device dimensions are right at the limit of the transparency mask making process, the fabrication result will somewhat differ from the intended outcome. As the exact results are not

quantifiable during the design process, a number of 48 different designs, each with only incremental changes, is designed. Design variations include differently shaped clutches as well as offsets of the two halves of the clutch in order to compensate for mask and fabrication inaccuracies. A total of 252 individual devices are arranged on one wafer. The devices are clustered in groups of six so that the wafer can be cut into dies of 10 by 10 millimeters for testing (Figure 5-3).

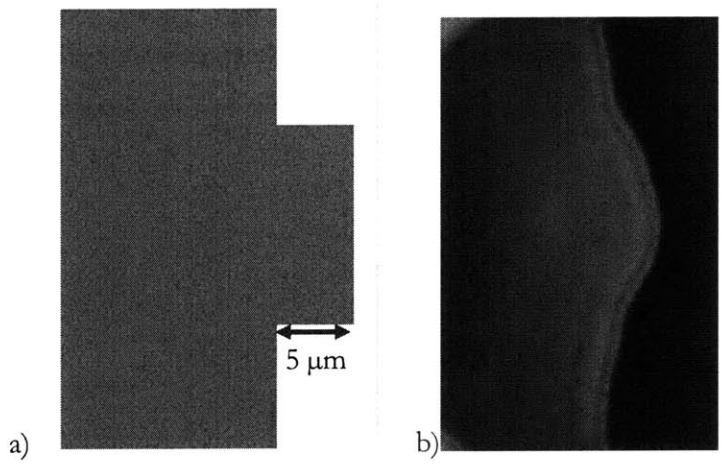

Figure 5-2: Discrepancy between initial design feature as part of the CAD drawing submitted to the mask making company (a) and the resulting feature as part of the SU-8 structure (b).

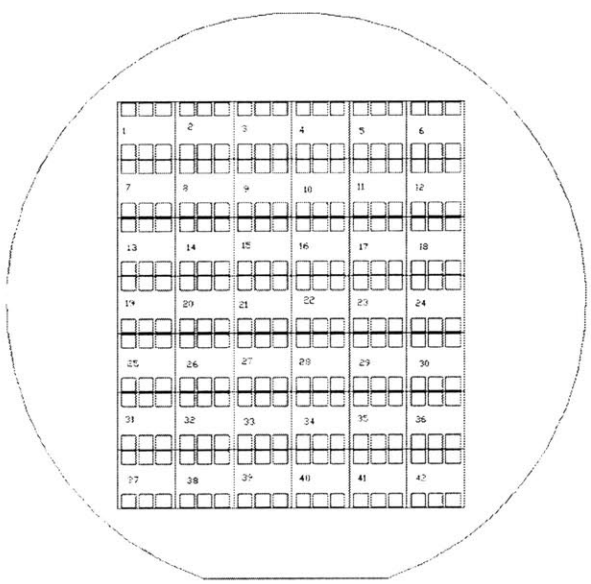

Figure 5-3: The individual devices are clustered in groups of six on 42 dies.

5.3 Step by Step Fabrication Process

5.3.1 Alignment Marks

As a first step, alignment marks are needed on the bare silicon wafer in order to align the masks for the subsequent manufacturing steps with respect to the wafer and to each other. Instead of the commonly used etching of alignment marks, metal deposition via e-beam evaporation is used to create marks which are easily visible through the various resists which are spun on in the following steps. During the same process step a series of numbers is marked on the wafer in order to facilitate navigating through the forty-two individual dies.

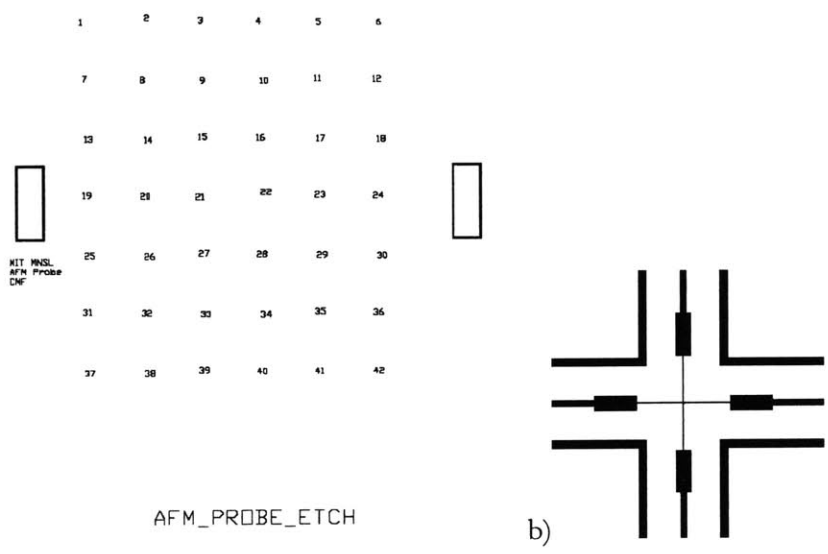

Figure 5-4: Mask layout for the alignment marks (a) and close-up view of the alignment mark (b)

Table 5-1: Process parameters for the metal deposition of the alignment marks.

Step #	Description	Parameters
1	Image Reversal Photoresist for Metal Lift-Off	Thickness: 1.2 μm Spin Speed: 1,400 rpm Softbake: 30 min @ 90°C Exposure: 2 sec Hardbake: 30 min @ 90°C Flood Exposure: 60 sec
2	Gold Deposition	Thickness: 100 nm Deposition Rate: 0.3 nm/sec
3	Metal Lift-Off	Immersion in Acetone Bath for 12 hrs

5.3.2 SU-8 Structure

The SU-8 layer is spun on with a thickness of 15 μm. After a short softbake to evaporate the solvent, it is UV exposed to activate crosslinking of the structure. It is followed by a post-exposure bake to further crosslink the device which can be developed afterwards in PM Acetate. In order to maximize structural integrity and rigidity, the device is hardbaked for 12-14 hrs at 90°C. The result can be seen in Figure 5-6.

SU-8 has been chosen as a structural material because it allows easy and reliable fabrication of any shape without additional etching. Furthermore it offers a high mechanical strength and flexibility and its low Young's modulus of 4 GPa helps to achieve a low overall probe stiffness.

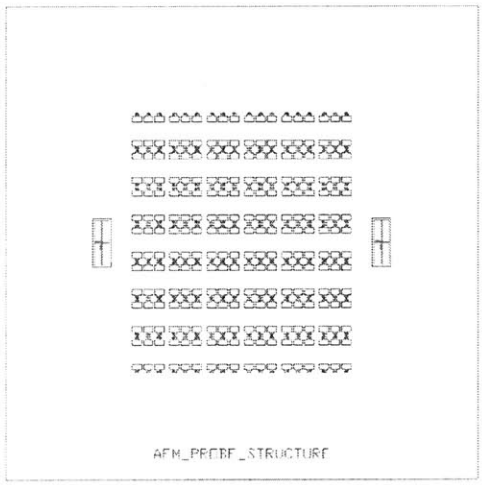

Figure 5-5: Mask layout of the SU-8 process.

Table 5-2: Process parameters of the SU-8 process.

Step #	Description	Parameters
4	Spin-On SU-8	Spin Speed: 3,000 rpm Softbake: 1.5 min @ 65°C, 3 min @95 °C Exposure: 2 x 5.5 sec Hardbake: 3 min @ 65°C, 3 min @ 95°C
5	Develop SU-8	2 min PM Acetate Bath, 0.5 min PM Acetate Rinse, 1 min Isopropanol Rinse, Blow Dry
6	Hardbake SU-8	12 hrs @ 95°C

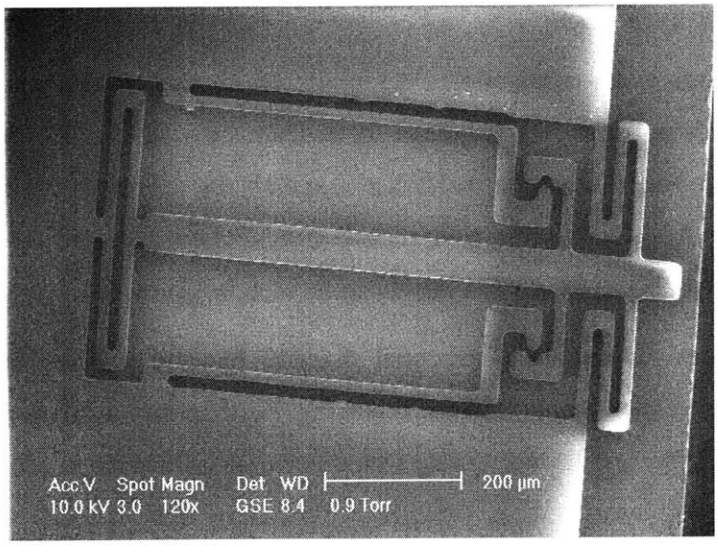

Figure 5-6: SEM picture of the SU-8 structure of the AFM probe.

5.3.3 XeF_2-etch to create undercut

In the next step the device undergoes a timed XeF_2-etch which selectively etches the silicon base. This creates a slight undercut preventing the metal layer which is deposited later to connect the sidewalls with the substrate (Figure 5-7).

Table 5-3: Process parameters for the XeF_2 undercut etch.

Step #	Description	Parameters
7	XeF_2-Etch	Etch Time per Cycle: 30 sec Number of Cycles: 5

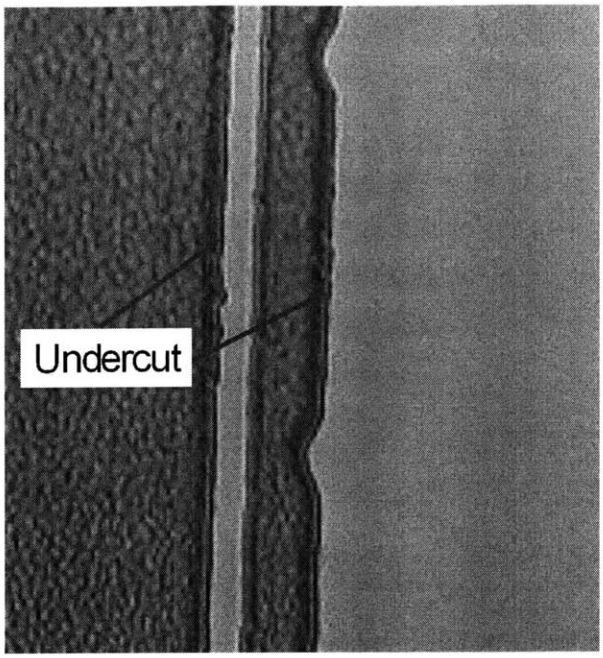

Figure 5-7: Top view of the undercut. The XeF_2-etch has produced a 2μm-undercut which can be seen as dark lines through the clear SU-8.

5.3.4 Electrodes

Thick lift-off resist is spun on and patterned to create a mask for the metal layer. Development of the resist is difficult because of the deep trenches formed by the SU-8. In order to ensure proper development several layers are spun on to increase the resist thickness, exposure times are increased, and the resist is developed in an ultrasonic bath.

Gold is deposited via e-beam evaporation to form the actuators on the sidewall of the SU-8 structure as well as the electrical connections. To improve adhesion of the metal to the SU-8 a 25 nm thin titanium layer is deposited between the gold and device. The release layer is then dissolved in acetone to lift off the excess metal. The result can be seen in Figure 5-9.

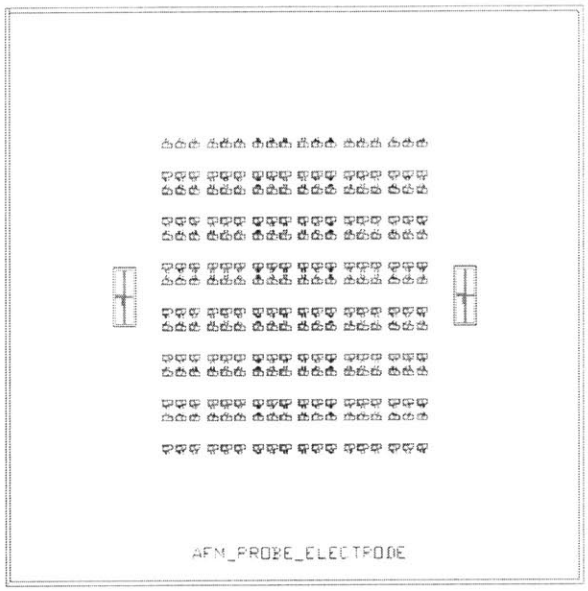

Figure 5-8: Mask layout for the metal deposition of the electrodes.

Table 5-4: Process parameters for the metal deposition of the electrodes.

Step #	Description	Parameters
8	Image Reversal Photoresist for Metal Lift-Off	Thickness: 5.5 µm Spin Speed: 1.200 rpm Softbake: 30 min @ 90°C Exposure: 6 sec Hardbake: 30 min @ 90°C Flood Exposure: 150 sec
9	Metal Deposition	Chromium: 20 nm @ 0.2 nm/sec Gold: 200 nm @ 0.3 nm/sec
10	Metal Lift-Off	Immersion in Acetone Bath for 36 hrs

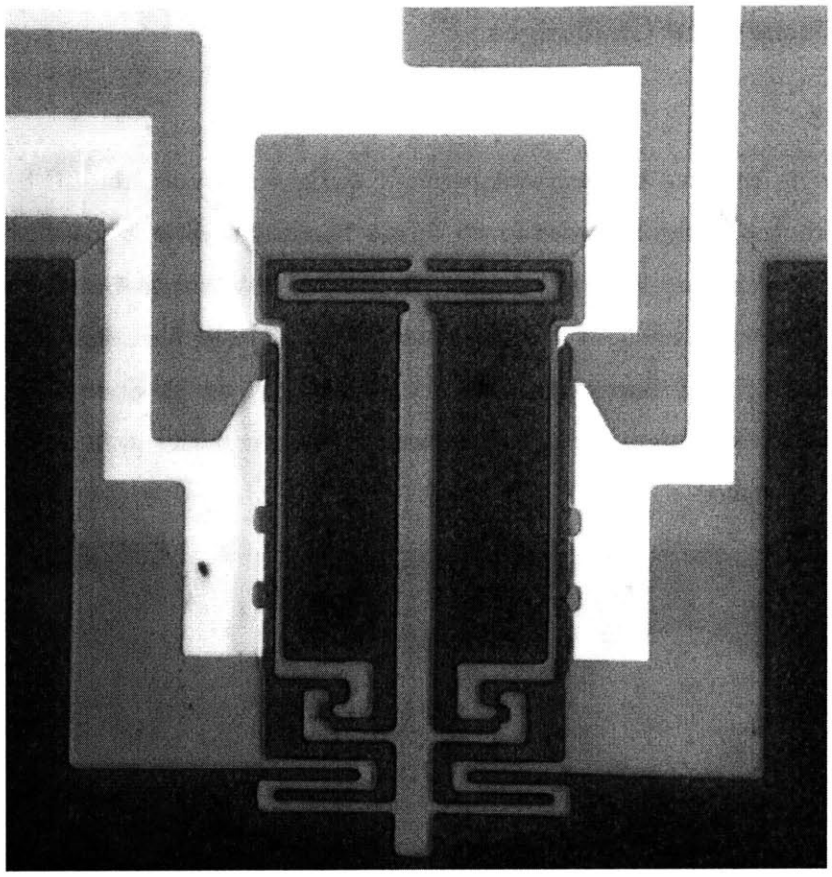

Figure 5-9: Top view of the SU-8 structure with gold electrodes.

5.3.5 XeF_2 Release Etch

In a last step the device undergoes a second XeF_2-etch to release the moving parts of the structure from the silicon wafer.

Table 5-5: Process parameters for the XeF_2 release etch.

Step #	Description	Parameters
11	XeF_2 Release Etch	Etch Time per Cycle: 30 sec Number of Cycles: 40

5.4 Issues and Challenges

5.4.1 SU-8

In order to produce devices with perfectly straight sidewalls, the SU-8 needs to be exposed homogeneously. In order to do this, a bandwidth filter is installed for spectral shaping of the exposure light. It removes the shorter wavelengths below 350 nm which would be absorbed primarily in the upper portion of the resist film, resulting in negatively sloped sidewalls (called T-topping). Figure 5-10 (a) shows an SU-8 structure with sloped sidewalls, due to exposure without the bandwidth filter, the device in (b) has been exposed with the filter installed.

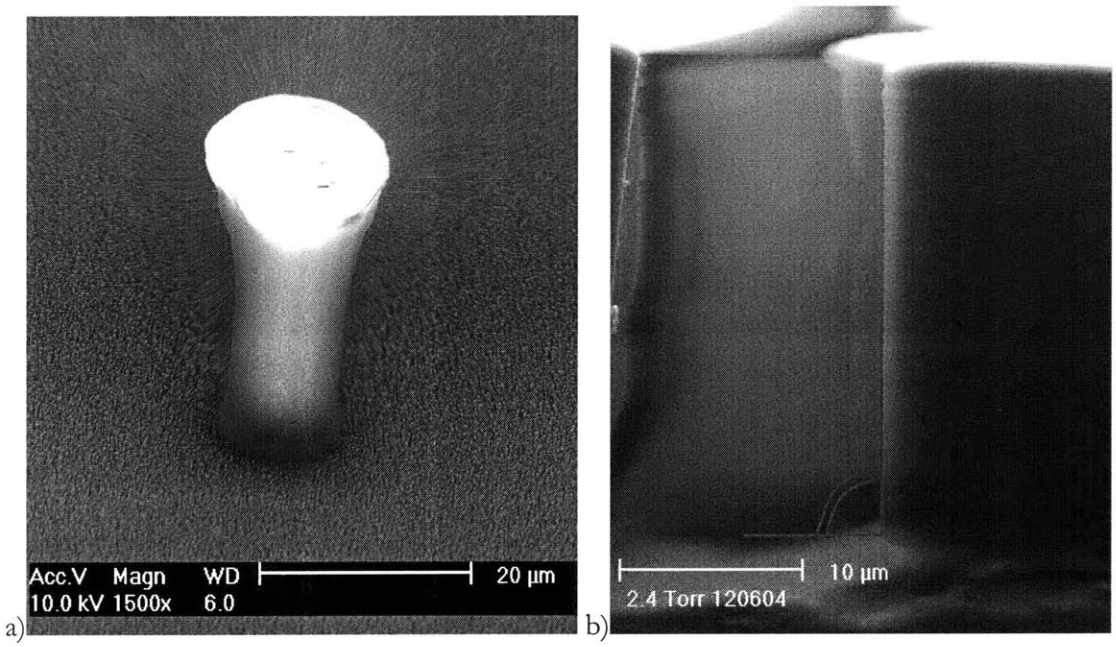

Figure 5-10: SU-8 structure with sloped sidewalls (a) and with perfectly straight sidewalls (b).

Another issue requiring special attention is the build up of stress within the SU-8. Due to the evaporation of the solvents during the softbake and the cross linking of the polymers during exposure and post-exposure bake, the SU-8 shrinks. This, in combination with the difference of the thermal expansion coefficients of the resist and the supporting wafers (SU-8: ~52 ppm/K, Silicon wafer: ~2 ppm/K) leads to stress which can cause cracking during manufacturing as well as buckling after the release of the device. Stresses of up to 19 MPa

have been reported [49]. In order to ensure the integrity of the device, the temperature is tightly controlled and slowly ramped up and down before and after the various baking steps.

5.4.2 Electrode Lift-Off

The main challenge during fabrication was to perfect the lift-off process. In order to produce metal sidewalls for the actuation of the clutches, the lift-off resist within the 20 μm deep trenches of the SU-8 has to be dissolved, while the thin resist on top of the device needs to remain. The selectivity of the developer for exposed and unexposed resist is not high enough to permit this. During the time it takes for the resist within the trenches to dissolve, the resist on top of the device will be gone as well. As a solution, several layers of lift-off resist are spun on, which quintuples the thickness of the resist on top of the device (from 1.2 μm to 6 μm), but adds only another 20 % on top of the 20 μm trenches (from 20 μm to 24 μm). Several timed process parameters need to be adjusted in order to find the right combination to achieve good results with this thick resist:

- A short bake after the deposition of each layer is needed in order to create a crust for the spin-on of the following layer. Already small changes in time have a big effect on development time and resist quality. A bake time of two minutes has proven to be optimal.
- The exposure time with the mask for the electrodes needs to be significantly increased to six seconds due to the thickness of the resist.
- The flood exposure time is critical in order to activate the parts of the resist which need to be dissolved. It has been increased to 150 seconds.
- The development time needs to be prolonged to completely dissolve the resist within the deep trenches but has to be short enough to leave a sufficiently thick resist on top of the device to perform the lift-off. Seven to seven and a half minutes are optimal. A very short ultrasonic treatment on low power can be used to improve the development.

5.4.3 XeF_2 Release Etch

The release etch can damage the AFM probe and destroy the metal connections. In order to improve the durability of the device, the adhesion layer material between the SU-8 and the gold has been switched from titanium to chromium. In addition, at least ten silicon

dies should be etched in the XeF_2 chamber at once; otherwise the gas concentration around the individual device is too high which can result in a complete metal lift-off.

5.5 Results and Summary

A high-quality SU-8 structure without cracks and air bubbles in the device is routinely produced. The sidewalls of the device are straight with a 90° angle, as seen in Figure 5-10 b, a prerequisite for producing the electrostatic actuators for engaging the clutches in a lift-off process. A recipe has been found which optimizes the parameters of the lift-off resist process, allowing for the fabrication of solid metal coatings on the sidewalls. The following figures detail the processing results.

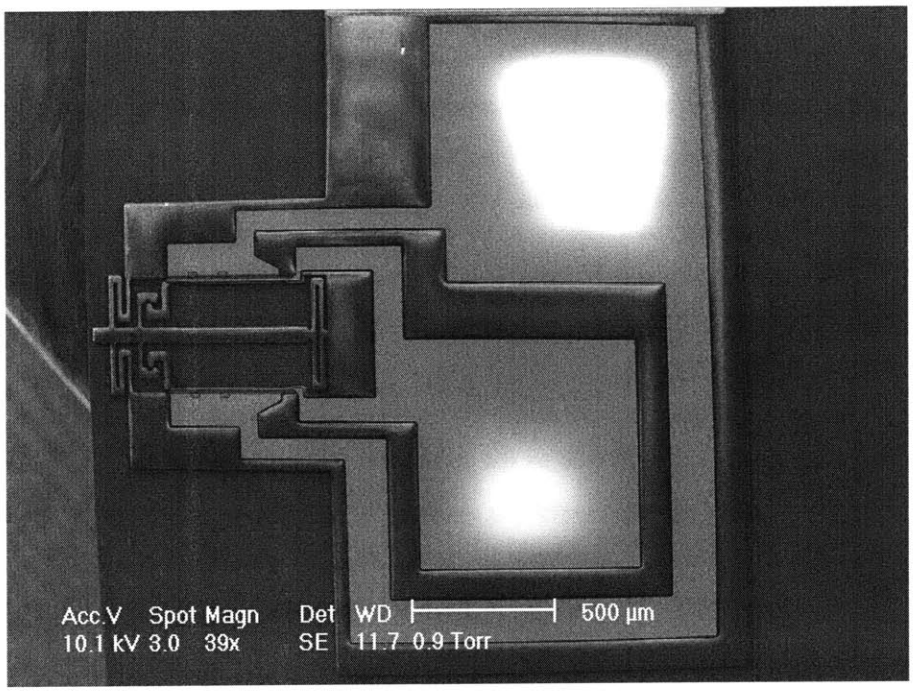

Figure 5-11: Top view of the unreleased device. The AFM probe can be seen on the left, the right shows the metal pads which provide ample surface area to make electrical connections with the actuator.

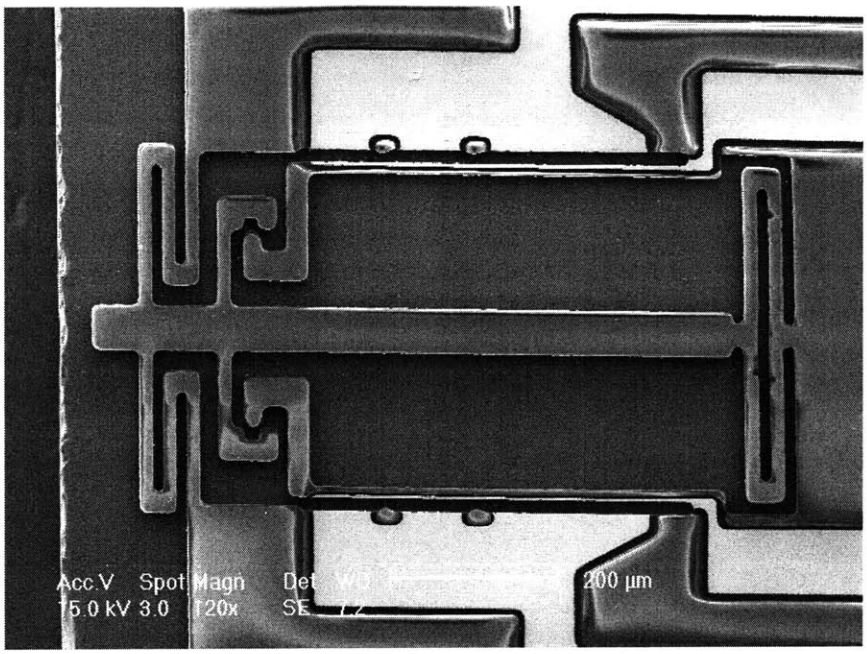

Figure 5-12: Top view of the unreleased AFM probe.

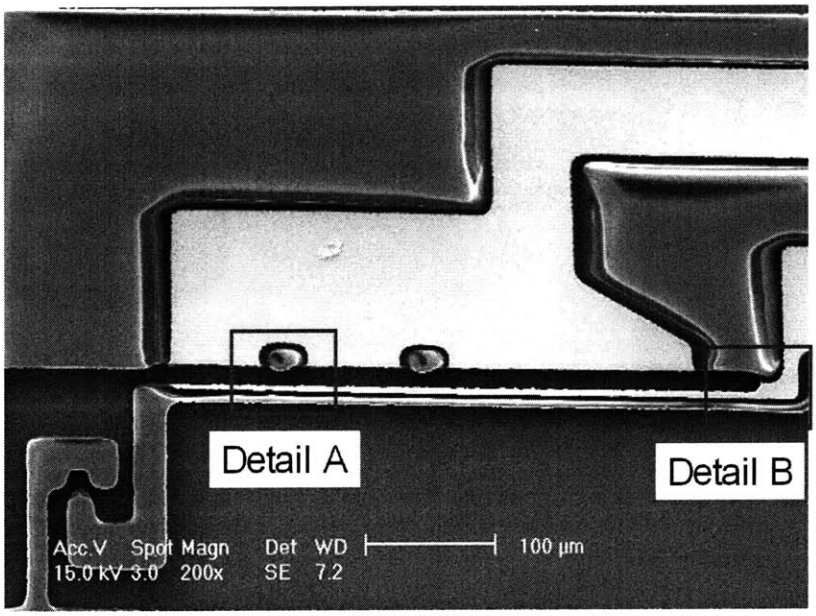

Figure 5-13: Top view of one side of the AFM probe, showing the electrostatic actuator and the clutch. Details A and B are shown in Figure 5-14 and Figure 5-15.

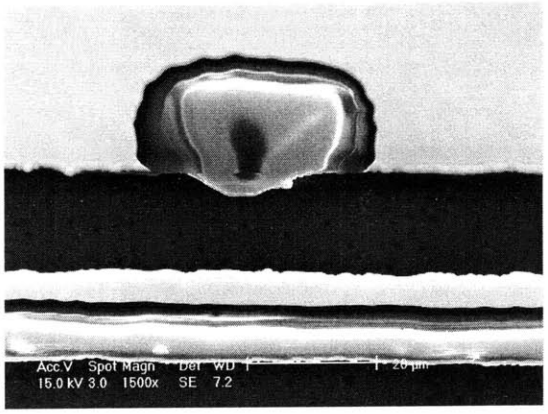

Figure 5-14: Detail A from Figure 5-13 above.

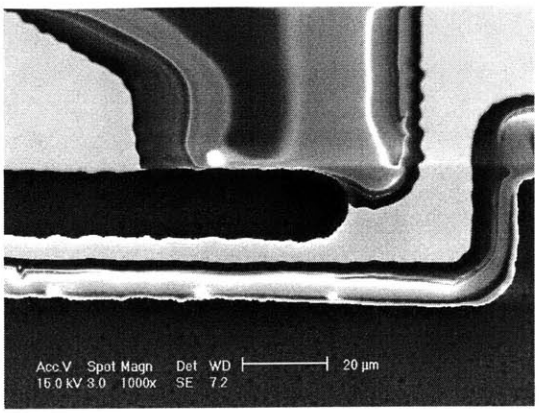

Figure 5-15: Detail B from Figure 5-13above.

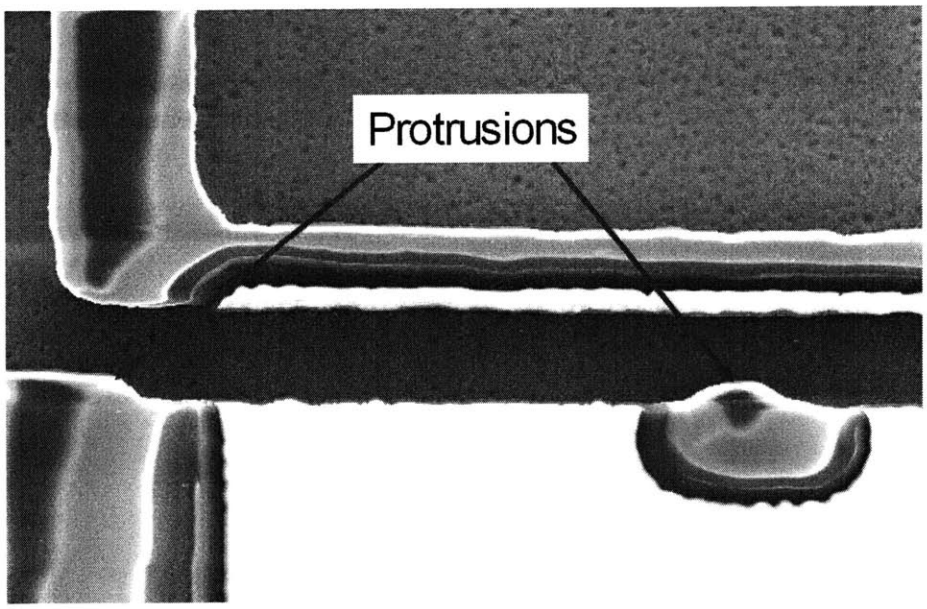

Figure 5-16: The protrusions are not covered with metal. They stick out of the sidewall in order to prevent a short circuit resulting from contact of the two sides of the electrostatic actuator.

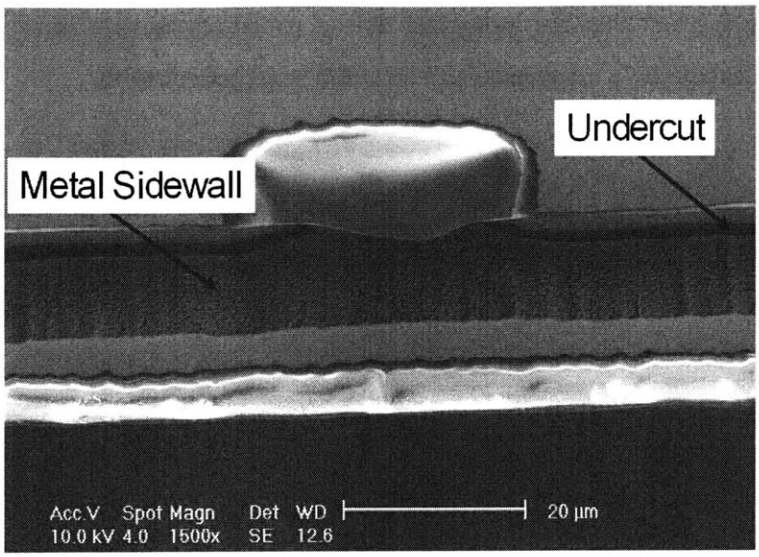

Figure 5-17: Angled picture to reveal the metal sidewall and the undercut.

The fabrication results show that transparency masks are sufficiently capable for this process. Comparing the intended beam width of the flexures of the device (as drawn in the CAD model and submitted to the mask making company) to the resulting beam width of the SU-8 structure reveals a discrepancy of 45 % (14.5 µm instead of 10 µm). This stems mostly from the required transfer of the pattern of the transparency mask to a chrome-glass mask, which is needed for the processing in the lab, and from the edge roughness of the mask which creates wider structures in SU-8. This is not a problem for the proof-of-concept, though, as the exact specifications are of minor importance. The stiffness model in section 4.4 has been recalculated with the change in dimensions included.

The processing results are inhomogeneous across the wafer, resulting in a limited number of functional devices out of the on one wafer. The processing steps are highly sensitive to small changes of the processing parameters, but manual handling and deficiencies in processing equipment as well as challenges which arise from the small size of the devices make more reliable fabrication difficult. Uniform heating, for example, which is required during a number of process steps, is made impossible by curved surfaces of the available hotplates and frequent opening of the baking ovens by other lab users. This results in uneven development of the lift-off resist, which, as a consequence, defeats any possibility of performing a quality metal lift-off across the whole wafer. The tolerances for lift-off thickness are very tight and metal adhesion is not very strong. The manual lift-off is further

complicated by the fact that the individual device structures are too small to be observed during lift-off, leaving only experience and intuition as judgment tools.

6. Device Testing and Discussion

6.1 Clutch performance

The performance of the electrostatic actuation and the clutch is examined with the RF-1 Microwave Probe Station shown in Figure 6-1. First, the tip of the released AFM probe is manually pushed in order to verify that the middle part can move freely in disengaged state. Afterwards the voltage supplied by the KEPKO 500M bipolar high voltage power supply is slowly increased. Movement of the electrostatic actuator starts at around 220 volts and the clutch is fully pulled in at 300 volts. The tip is manually moved again in order to test if the clutches provide a secure fit without slipping. Reducing the voltage in the final step disengages the clutches.

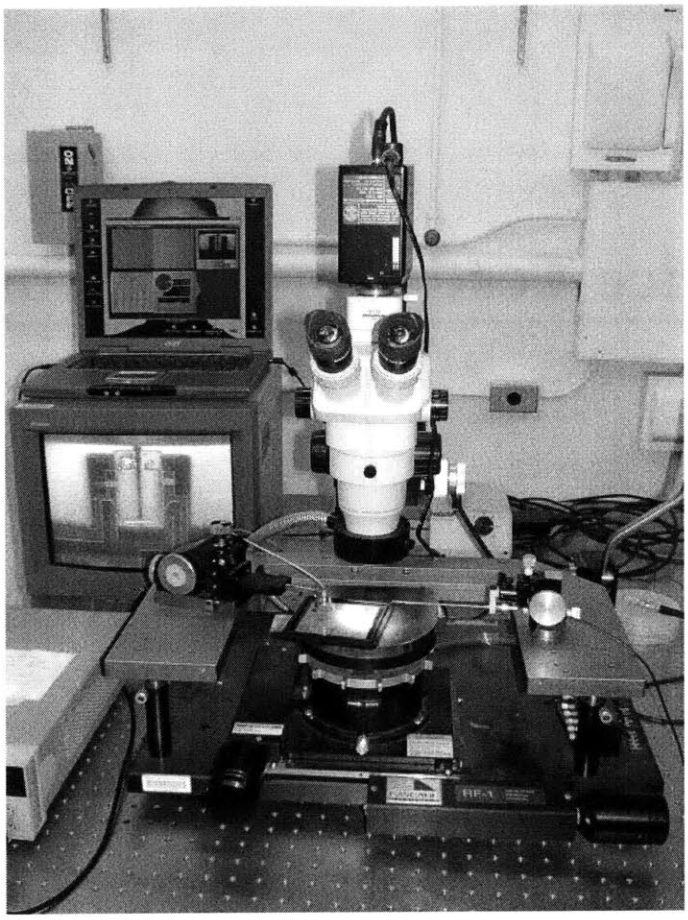

Figure 6-1: Microwave probe station used to test the performance of the electrostatic actuated clutches.

The tests show that the actuation works flawlessly as long as the applied voltage is high enough. The two parts of the clutch fit together and stay securely engaged without slipping (Figure 6-2). Disconnecting the voltage reliably disengages the clutches, no sticking is observed.

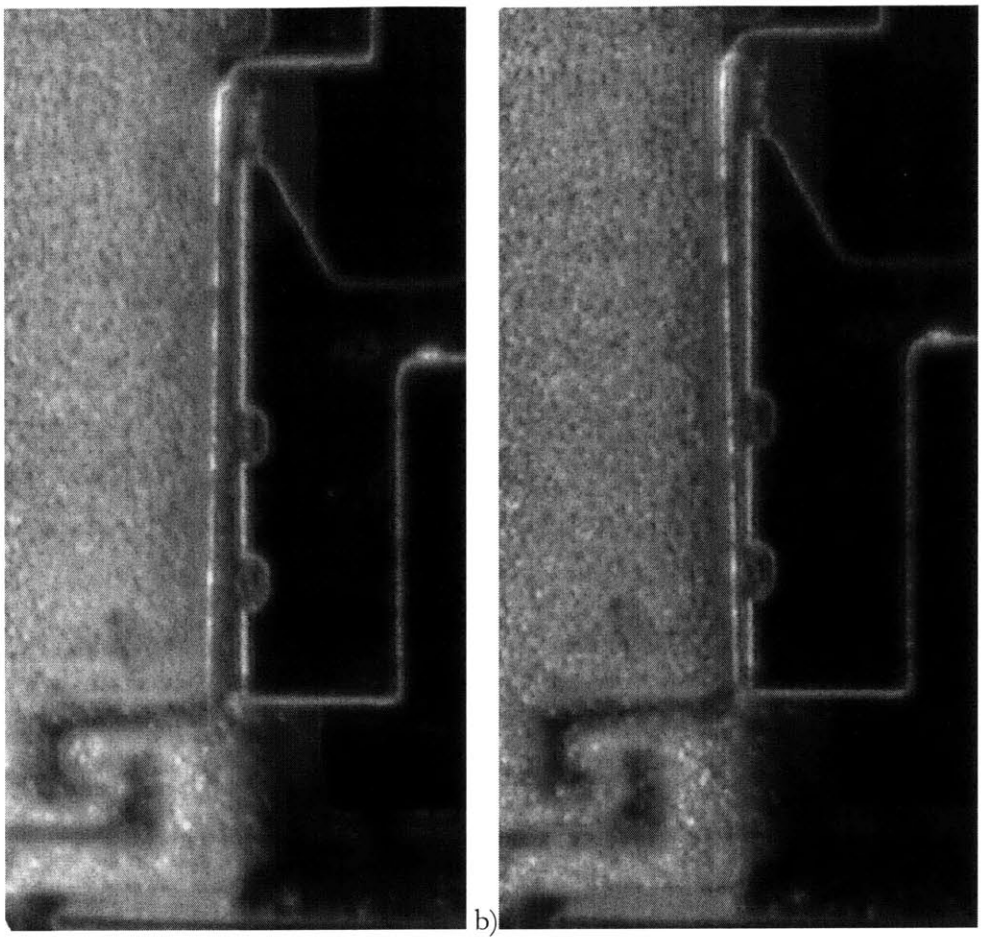

Figure 6-2: Clutch disengaged (a) and engaged (b). As the SU-8 is clear, the structure is difficult to see against the dark background. The black shapes seen on the wafer are not the device itself but only its silhouette resulting from the XeF_2 release etch. The glaring of the gold however shows the position of the clutch and clearly shows it is pulled in.

The high value of the required voltage (compared to the calculated 135 volts in section 4.5) stems from the fact that the beam width of the actual device is significantly higher than intended, due to inaccuracies introduced by the mask making and pattern transfer process described in section 5.2. As a result, voltage breakdown has occasionally been observed, resulting in the destruction of the device.

Because of the design variations of the 252 individual devices, only a limited number of devices per wafer have the correct dimensions to function properly. The inhomogeneity of the fabrication results further reduces the number of functioning devices. Some show not fully released metal, others exhibit excessive metal lift-off. Ablation of the metal on the sidewall of the electrostatic actuators during actuation has been observed as well.

6.2 Stiffness measurement of the AFM probe

The actual stiffness of the device is crucial in meeting the requirements with regard to the scanning of biological samples. In order to verify the results from the lumped element model in section 4.4, the device is tested with the Hysitron Triboindenter® nanoindentation transducer (schematic shown in Figure 6-3). The nanoindenter provides a maximum tip displacement of 5 μm with a resolution smaller than 0.002 Å and a load range of 10 μN to 10 mN with a resolution better than 1 nN.

The indenter uses a sharp tip to probe a sample which is fixed on top of a piezo scanner. The tip is suspended by a threeplate capacitive transducer (Figure 6-3) which acts as an actuator and sensor. The middle plate, which holds the tip, is supported by springs between two more plates. The outer plates are rigidly connected to the frame of the indenter. The bottom plate has a small hole which permits the tip to stick out. In order to move the tip, a voltage V_f is applied to the middle and bottom plate. This electrostatic actuation requires practically no current, eliminating drift from heating during actuation. The displacement can be simultaneously measured by the change in capacitance between the middle and top plate. This unique setup allows for the acquiring of force-displacement curves, from which the stiffness of the AFM probe can be calculated.

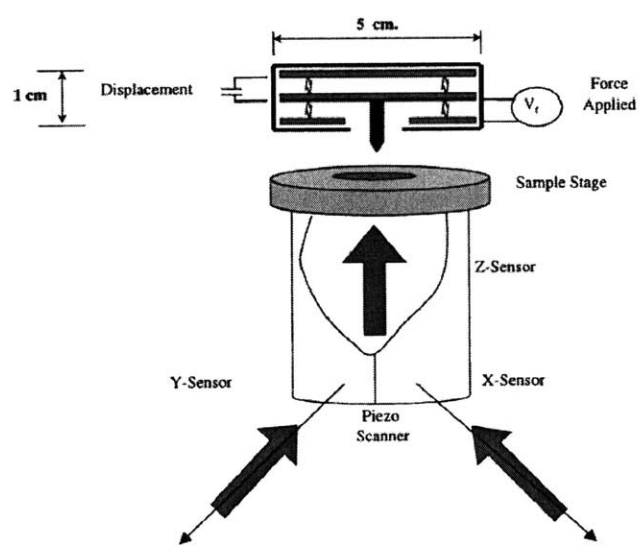

Figure 6-3: Schematic view of the functional elements of the Hysitron Triboindenter® [50].

In order to isolate the test setup from the environment, ambient noise and vibrations are dampened by active piezoelectric vibration control (for vibrations under 200 Hz) and passive vibration damping (for vibrations over 200 Hz). The full enclosure shown in Figure 6-4 provides additional protection from environmental influences.

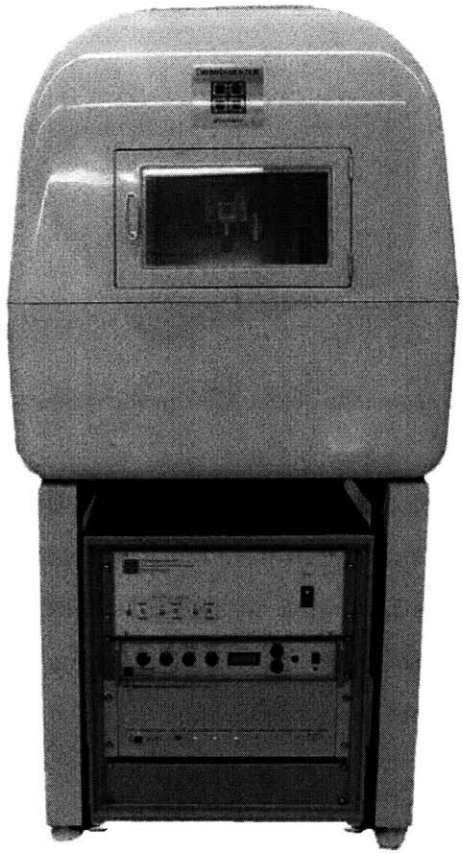

Figure 6-4: Outside view of the Hysitron Triboindenter® [51].

For the interpretation of the results, a number of assumptions are made about the testing process. First of all, the compliance of the nanoindenter is negligible compared to the deflection of the AFM probe. This is certainly true, as the stiffness of the nanoindenter is of the order of 10^6 N/m. Second, the indentation of the tip into the surface of the device is neglected. This can be done since the forces involved are less than 80 μN, which leads to an indentation in the range of a few nm. In contrast to this, the deflection of the device is of the order of hundreds of nm. Third, the angle between tip and device surface is assumed to be perpendicular, resulting in a probe deflection along the axis of tip displacement. In order to

ensure this, a fixture is machined, which correctly aligns the silicon die (10 mm x 10 mm) that carries the AFM probe, with respect to the sample holder of the indenter (Figure 6-5).

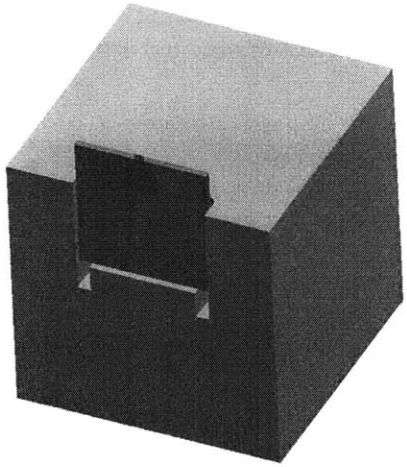

Figure 6-5: Fixture for correct alignment of the AFM probe during stiffness measurement with the nanoindenter.

The load-time curve applied by the indenter can be seen in Figure 6-6. In order to account for creep, to minimize vibrations from initial contact, and to let the tip settle on the surface of the device, the tip is kept stable without movement at the point of contact for 10 seconds. Then a force of close to 54 μN is applied over a time span of 20 seconds and released over the time of another 20 seconds.

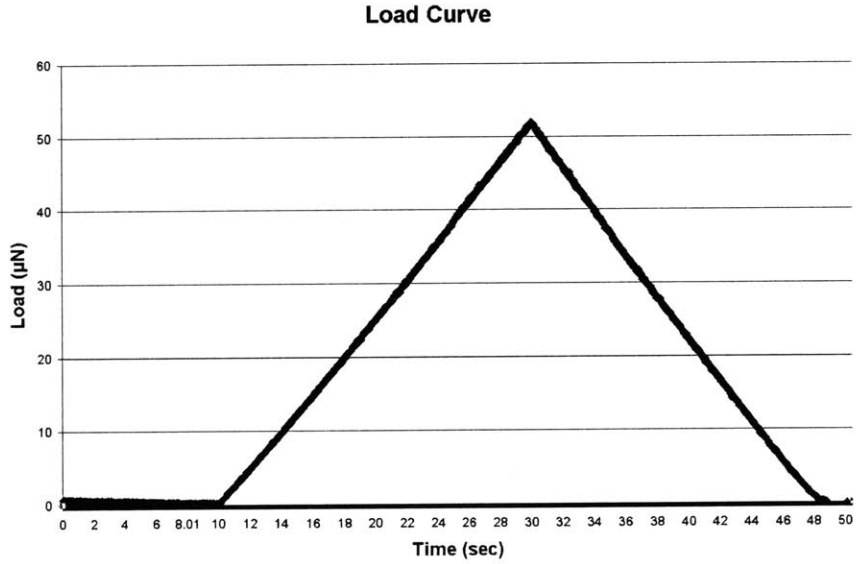

Figure 6-6: Load-time curve for the stiffness measurement cycle.

Figure 6-7 shows the force-displacement curve for the low stiffness mode (clutches disengaged) of the AFM probe. Three separate measurements have been taken and an average stiffness of k_{low} = 56.8 N/m is calculated from these results. This is close to the 53.7 N/m which has been calculated with the lumped element model approach introduced in section 4.4.

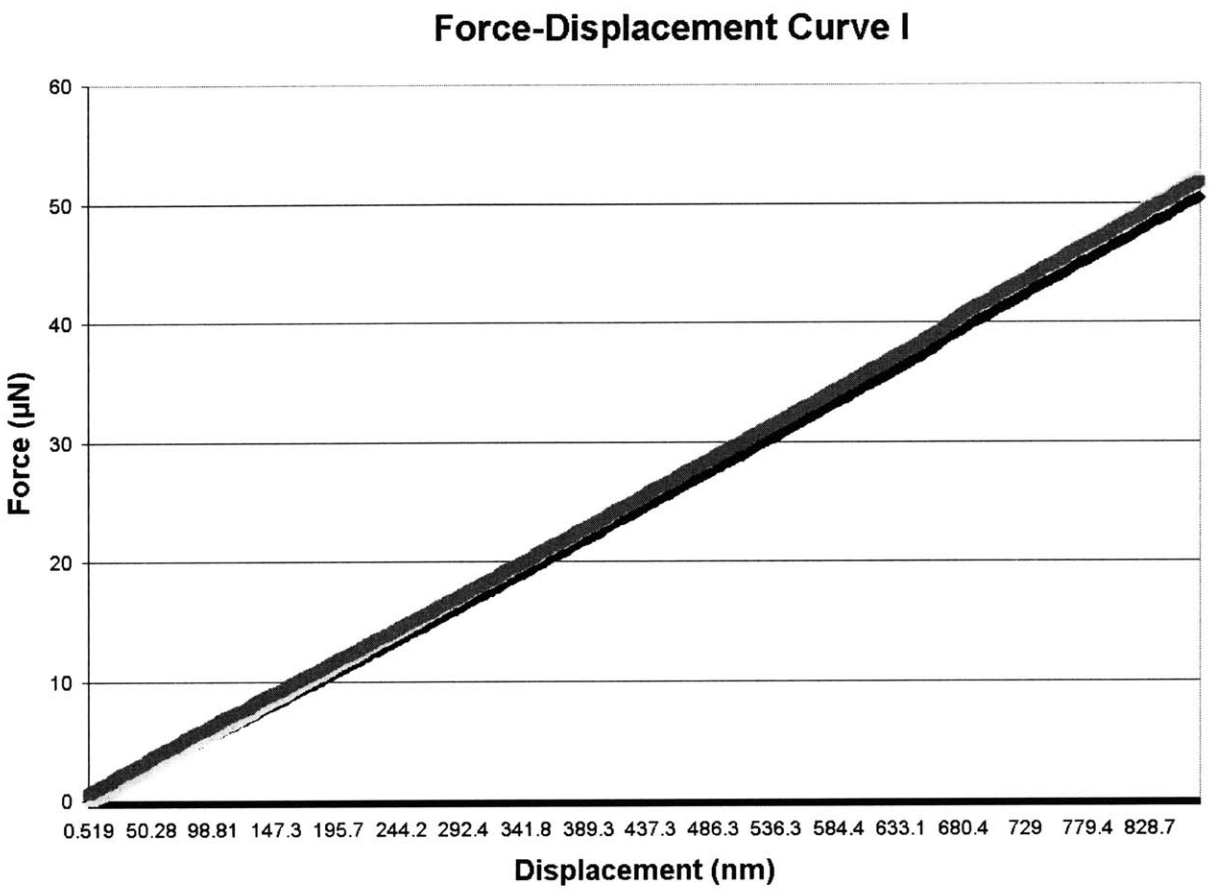

Figure 6-7: Force-displacement curve of the AFM probe with clutches disengaged.

Figure 6-8 shows the force-displacement curve of the high stiffness mode (clutches engaged) of the AFM probe. Again, three separate measurements have been taken. An average stiffness of k_{high} = 97.3 N/m is calculated, which differs slightly from the calculated value of 122 N/m.

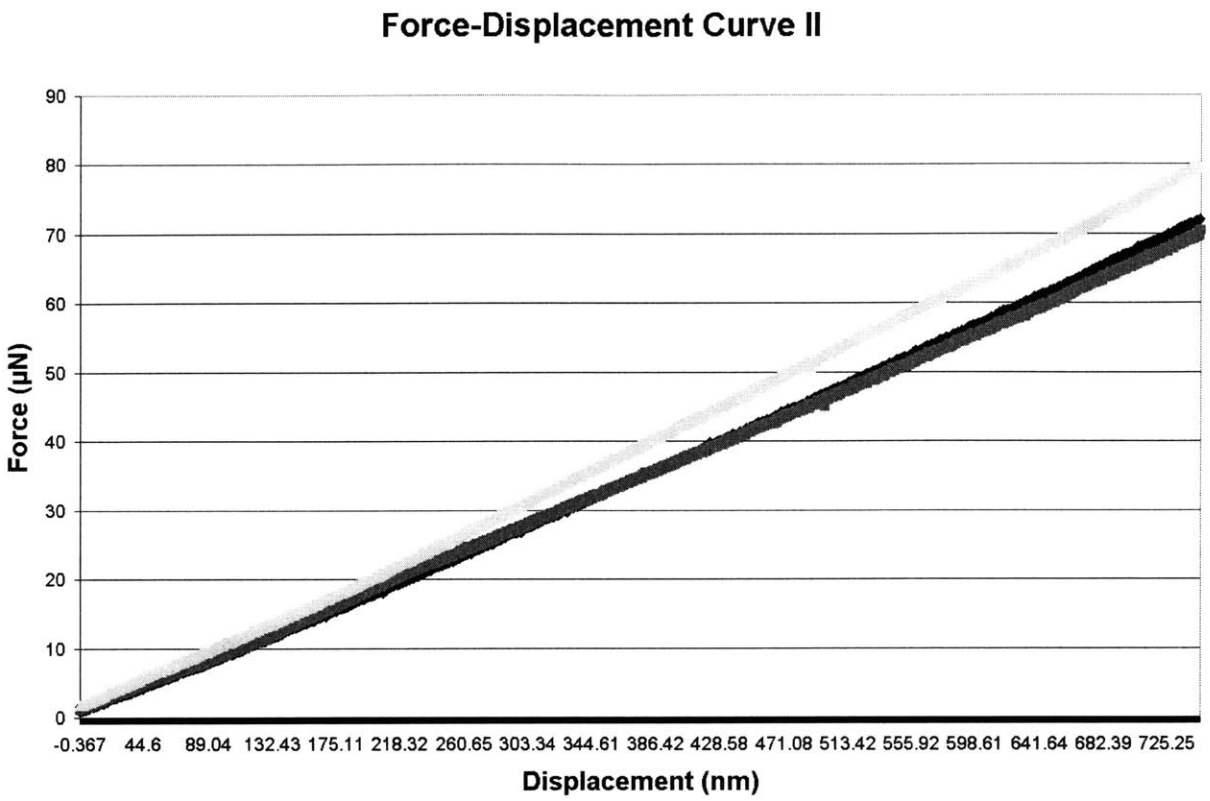

Figure 6-8: Force-displacement curve of the AFM probe with clutches engaged.

7. Conclusion and Future Work

7.1 Conclusion

This thesis discusses the requirements of scanning probes for biological applications, as deduced from current AFM practices and their shortcomings with regard to the special challenges presented by *in vivo* sampling of living cells. Based on this, a novel in-plane AFM probe has been designed. It features a switchable stiffness which makes adaptive scanning of the varying hardness surface of biological samples possible. In addition, the in-plane design will facilitate system integration across scales from nano to micro and the building of massively parallel arrays. In order to calculate the optimal stiffness for the scanning of biological samples, the tip-sample interaction force and the indentation of the tip into the sample have been modeled. A manufacturing process with standard MEMS fabrication steps has been conceived and optimized for the fabrication of the proof-of-concept device of the switchable stiffness model. The same manufacturing process can be used for the fabrication of the device with the final stiffness values as well. The clutch performance has been tested successfully. The dual stiffness, measured via nano-indentation, agrees well with the predicted values.

7.2 Future Work

As for a next step, the design should be scaled down in order to achieve the low stiffness required for biological applications. The manufacturing process will essentially be the same, but chrome-glass masks, instead of the transparency masks, have to be used in order to achieve the necessary feature size. A beam width of 1-2 μm is the smallest possible size which is manufacturable with the equipment currently available at the Microsystems Technology Laboratories. For this, the beam length and overall device dimensions have been calculated to achieve the desired stiffness.

In order to build a functioning AFM probe system, a capacitive sensor should be integrated to measure the tip movement, which is not included in the proof-of-concept device. The same process step as for the fabrication of the electrostatic actuators can be used. The design of the sensor simply has to be incorporated in the layout of the mask for the metal lift-off. The tip can be integrated by using a RIE etch to produce a groove at the front end of the device, followed by manual assembly of the nanocandle, as described in section 3.4.

More testing with regard to clutch performance and dynamic device behavior under real world applications should be conducted. This includes examining the effect of engaging the clutch on tip position. As an ideal case, the tip position should not change at all, regardless of the status of the clutch, since the device is designed to be symmetric. In addition, the opening and closing of the clutch should be investigated while the tip is moving.

7.3 Promising Applications

7.3.1 Protein Printing

The miniaturization of bioanalytical processes, bringing together biology, chemistry and MEMS in the field of BioMEMS, has a very promising application in the form of protein biochips.

This miniaturization makes the identification of thousands of analytes in only a few microliters of a biological sample possible. Applications range from drug development, clinical diagnosis, and early disease detection to studying molecular mechanisms of biological processes [52].

A biochip carries as the active element organic or biological specimens, arrayed in microdroplets of various shapes. Smaller individual droplets enable the testing for an increased number of characteristics with a minimized amount of fluid sample while keeping the required chip surface constant. These two-dimensional arrays enable massively parallel analyses of complex biological samples.

While various methods of building protein micro-arrays exist, two major ones are most heavily investigated. The first one uses a setup similar to that of an AFM probe, with a sharp tip which is wetted by dipping into a solution and then brought in contact with the surface in

order to deposit a microdroplet (dip-pen printing). The other one involves a dispensing system which deposits microdroplets from a fluid reservoir in a non-contact style similar to inkjet printing (drop-on-demand printing).

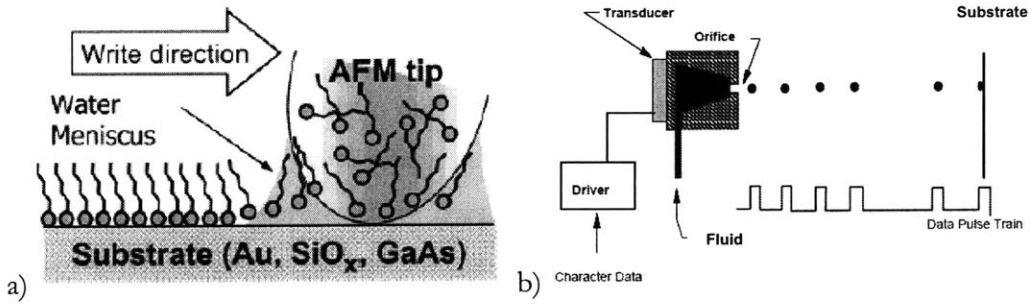

Figure 7-1 (a) Schematic diagram illustrating dip-pen nanolithography: A tip coated with "ink" molecules was brought into contact with the substrate. A water meniscus formed between the tip and the substrate, which facilitated the transport of the ink to the substrate [53]. (b) Diagram of drop-on-demand printing: Droplets of fluid are released from a reservoir through an orifice [54].

Dip-pen printing does not provide a steady fluid flow – frequent recoatings of the tip are necessary due to the lack of a reservoir. The coating process itself, done by dipping the tip into the solution is complicated and not very reliable, resulting in poor repeatability of the printing process. Current drop-on-demand printing methods, on the other hand, suffer from poor placement accuracy of the droplets and complex system architecture, which makes system integration, the building of arrays, and manufacturing difficult.

Here our novel design of the in-plane AFM probe offers significant advantages. In the next step the integration of fluid channels is planned. SU-8 as a structural material has already been successfully used for the fabrication of fluidic bioMEMS devices as it allows for multiple stacked coatings and can even be used for a secure sealing of the channels. The solution can then be deposited through a hollow carbon nanotube at the exact location desired. This device offers the following benefits with respect to the application of protein printing:

- easy fabrication by in-plane surface micromachining processes
- combined tool for imaging and delivering of fluids
- high accuracy and repeatability due to the functional integration of sensing and actuation

- overcoming of the drawbacks of dip-pen printing like unsteady fluid flow by offering integrated fluid channels and reservoirs while offering higher accuracy and better resolution than drop-on-demand systems
- easy arrayability for massive multi-printing

7.3.2 Tip-enhanced Raman Spectroscopy

Tip-enhanced Raman Spectroscopy (TERS) is one of the ideal applications of the in-plane AFM probe with a nanocandle tip. Raman spectroscopy, which is a good tool for detecting characteristics of various types of samples, suffers from low signal density. As an alternative to Raman spectroscopy, in TERS, an apertureless scanning near-field optical microscopy is deployed, in which a modified AFM tip or STM tip is brought into contact with the sample surface. This approach provides highly localized enhancements and offers a uniform enhancement when scanning over the sample. The parameters that mostl influence the enhancement factors are the distance of the tip from the surface, the tip radius, the direction of illumination and the exciting laser frequency. Optical quality of the tip is essential, and a tip with a smooth surface and a sharp end, and small tip radius is ideal for the tip-enhanced Raman processes. Ag, Au, and Cu are the materials currently used as metal tips in TERS.

The variable stiffness AFM probe can work as a tool for placing the tip close to a biological sample in order to enhance the Raman signals, and it provides a high bandwidth for lateral vibration, which is a requirement for TERS. A metal coated Carbon Nanotube (CNT) with a small diameter tip and high aspect ratio is ideal for this. A schematic of the in-plane system for TERS is shown below in Figure 7-2.

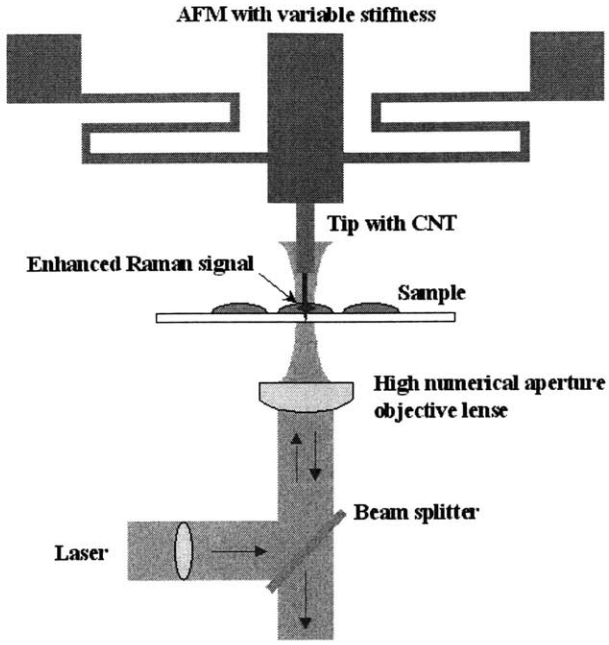

Figure 7-2: Schematic view of the in-plane AFM system used for TERS.

Bibliography

[1] Y.K. Kim, J. M. Bae, S.Y Son, J.H. Choi, S.G. Kim, "High speed atomic force microscope cantilevers with built-in piezoelectric actuator", IEEE Int. Conf. on Opt. MEMS, 1999

[2] S.C. Minne, S.R. Manalis, C.F. Quate, "Parallel atomic force microscopy using cantilevers with integrated piezoresistive sensors and integrated piezoelectric actuators", Appl. Phys. Lett. 67, pp. 3918-3920, 1995

[3] C.F. Quate, "Scanning probes as a lithography tool for nanostructures", Surface Science 386, pp. 259-264, 1997

[4] T. Ando, N. Kodera, Y. Naito, T. Kinoshita, K. Furuta, Y.Y. Toyoshima, "A high-speed atomic force microscope for studying biological macromolecules in action", Japanese Journal of Applied Physics 41, pp. 4851-4856, 2002

[5] P.C. Yang, Y. Chen, M. Vaez-Iravani, "Attractive-mode atomic force microscopy with optical detection in an orthogonal cantilever/sample configuration", J. Appl. Phys. 71, pp. 2499-2502, 1992

[6] J.A. Harley, T.W. Kenny, "A high-stiffness axial resonant probe for atomic force microscopy", J. Microelectromech. Sys. 10, pp. 434-441, 2001

[7] A. Majumdar, J.P. Carrejo, "Thermal imaging using the atomic force microscope", J. Appl. Phys. Lett. 62, pp. 2501-2503, 1993

[8] H. Bluhm, A. Wadas, R. Wiesendanger, K.-P. Meyer, L. Szczesniak, "Electrostatic force microscopy on ferroelectric crystals in inert gas atmosphere", Phys. Rev. B 55, pp. 4-7, 1997

[9] Y. Martin, D. Abraham, H. Wickramasinghe, "High-resolution capacitance measurement and potentiometry by force microscopy", Appl. Phys. Lett. 52, pp. 1103-1105, 1988

[10] M. Hersam, A. Hoole, S. O'Shea, "Potentiometry and repair of electrically stressed nanowires using atomic force microscopy", M. Welland, Appl. Phys. Lett. 7, pp. 915-917, 1998

[11] S. Sundararajan, B. Bhushan, "Development of AFM-based techniques to measure mechanical properties of nanoscale structures", Sensors and Actuators A 101, pp. 338-351, 2002

[12] M. Jaschke, H.-J. Butt, S. Manne, H. E. Gaub, O. Hasemann, F. Krimphove, E. K. Wolff, "The atomic force microscope as a tool to study and manipulate local surface properties", Biosensors and Bioelectronics 11, pp. 601-612, 1996

[13] M. Milani et al., "High resolution microscopy techniques for the analysis of biological samples: a comparison", Eur. Phys. J. Appl. Phys 26, pp. 123-131, 1994

[14] L. Haggerty, A. M. Lenhoff, "STM and AFM in Biotechnology", Biotechnol. Prog. 9, pp. 1-11, 1993

[15] P. Lehenkari, G. Charras, S. Nesbitt, M. Horton, "New technologies in scanning probe microscopy for studying molecular interactions in cells", Expert Reviews in Molecular Medicine, Cambridge University Press, 2000

[16] V.T. Moy, E.-L. Florin, H.E. Gaub, "Intermolecular forces and energies between ligands and receptors", Science 266, pp. 257-259, 1994

[17] M. Bezanilla, B. Drake, E. Nudler, M. Kashlev, P.K. Hansma, H.G. Hansma, "Motion and enzymatic degradation of DNA in the atomic force microscope", Biophys. J. 67, pp. 1-6, 1994

[18] Zhifeng Shao, Yiyi Zhang, "Biological cryo atomic force microscopy: A brief review", Ultramicroscopy 66, pp. 141-152, 1996

[19] P. P. Lehenkari, G. T. Charras, S. A. Nesbitt, M. A. Horton, "New technologies in scanning probe microscopy for studying molecular interactions in cells", Expert Reviews in Molecular Medicine 8, pp. 1-19, 2000

[20] A. L. Weisenhorn et al, "Deformation and height anomaly of soft surfaces studied with an AFM", Nanotechnology 4, pp. 106-113, 1993

[21] K. Kawabata et al, "Big softer hole on living cells: Elasticity imaging with AFM", Proceedings of SPIE 3922, pp. 91-98, 2000

[22] H. Haga, S. Sasaki, K. Kawabata, E. Ito, T. Ushiki, T. Sambongi, "Elasticity mapping of living fibroblasts by AFM and immunofluorescenceobservation of the cytoskeleton", Ultramicroscopy 82, pp. 253-258, 2000

[23] W. F. Heinz, J. H. Hoh, "Spatially resolved force spectroscopy of biological surfaces using the atomic force microscope", Tribtech. 17, 1999

[24] J. N. Israelachvili, "Intermolecular and Surface Forces", London: Acaemic, 1991

[25] B. Capella, P. Baschieri, C. Frediani, P. Miccoli, C. Ascoli, "Force-Distance Curves by AFM", IEEE Eng. in Med. and Bio. 16, pp. 58-65, 1997

[26] L. D. Landau, E. M. Livshits, "Theory of elasticity", Nauka, p. 246, 1987

[27] K.L. Westra, A.W. Mitchell and D.J. Thomson, "Tip artifacts in atomic force microscope imaging of thin film surfaces", J. Appl. Phys. 74, pp. 3608-3610, 1993

[28] K.D. Krantzman, D.C. Rees and D. Farrelly, "Computational study of the imaging of a molecular crystal with the atomic force microscope", J. Phys. Chem. 95, pp. 9039-9042, 1991

[29] U.D. Schwarz, "Tip artefacts in scanning force microscopy", J. Microsc. 173, pp. 183-197, 1994

[30] S. Banerjee, M.K. Sanyal, A. Datta, "Simulation study of multi-atom tips and estimation of resolution in atomic force microscopy", Appl. Surf. Sc. 99, pp. 255-260, 1996

[31] A. Boisen, O. Hansen, and S. Bouwstra, "AFM probes with directly fabricated tips", J. Micromech. Microeng. 6, pp. 58-62, 1996

[32] T.R. Albrecht, S. Akamine, T.E. Carver, C.F. Quate, "Microfabrication of cantilever styli for the atomic force microscope", J. Vac. Sci. Technol. A 8, pp. 3385-3396, 1990

[33] O. Wolter, T. Bayer, J. Greschner, "Micromachined silicon sensors for scanning force microscopy", J. Vac. Sci. Technol. B 9, pp. 1353-1357, 1991

[34] J.E. Griffith, D.A Grigg, M.J. Vasile, P.E Russell, and E.A. Fitzgerald, "Characterization of scanning probe microscope tips for linewidth measurement", J. Vac. Sci. Technol. B 9, pp. 3586-3589, 1991

[35] S. Iijima, "Helical microtubules of graphitic carbon", Nature 354, pp. 156-158, 1991

[36] M. Yasutake, Y. Shirakawabe, T. Okawa, S. Mizooka, Y. Nakayama, "Performance of the carbon nano-tube assembled tip for surface shape characterization" Ultramicroscopy 91, pp. 57-62, 2002

[37] S. Wong, J. Harper, P. Lansbury, C. Lieber, "Carbon Nanotube Tips: High-Resolution Probes fro Imaging Biological Systems", Journal of American Chemical Society 120, pp. 603-607, 1998

[38] H. Dai, J. Hafner, A. Rinzler, D. Colbert, R. Smalley, "Nanotubes as nanoprobes in scanning probe microscopy", Nature, Vol. 384, pp. 147-150, 1996

[39] http://www.piezomax.com/technology_2261.htm

[40] J. Hafner, C. Cheung, C. Lieber, "Growth of nanotubes for probe microscopy tips", Nature 398, pp. 761-762, 1999

[41] Sang-Gook Kim, US Patent Appl. No. 60/417,959

[42] S.D. Senturia, "Microsystem Design", Kluwer, 2001

[43] M. V. Gonzalez, "Dynamic Study of Tunable Stiffness Scanning Microscope Probe", Bachelor of Science Thesis at MIT, 2005

[44] H. Lorentz, M. Despont, N. Fahrni, P. Renaud, P. Vettiger, "SU-8: a low-cost negative resist for MEMS", J. Micromech. Microeng. 7, pp. 121-124, 1997

[45] H. Lorentz, M. Despont, N. Fahrni, J. Brugger, P. Vettiger, P. Renaud, "High-aspect-ration, ultrathick, negative-tone near UV photoresist and its applications for MEMS", Sensors Actuators A 64, pp. 33-37, 1998

[46] L. J. Guerin, M. Bossel, M. Demierre, S. Calmes, P. Renaud, "Simple and low cost fabrication of embedded microchannels by using a nes thick-film photoplastic", Proc. Transducers '97, pp. 1419-1426, 1997

[47] G. Genolet, M. Despont, P. Vettiger, D. Anselmetti, N. F. de Rooij, "All-photoplastic, soft cantilever cassette probe for scanning force microscopy", J. Vac. Sci. Technol. B 12, pp. 617-620, 2000

[48] I. Roch, P. Bidaud, D. Collard, L. Buchaillot, "Fabrication and characterization of an SU-8 gripper actuated by a shape memory alloy thin film", J. Micromech. Microeng. 13, pp. 330-336, 2003

[49] H. Lorentz, M. Laudon, P. Renaud, "Mechanical Characterization of a New High-Aspect-Ratio Near UV-Photoresist", Microelectronic Eng. 42, pp. 371-374, 1998

[50] J. D. Holbery, V. L. Eden, M. Sarikaya, R. M. Fisher, "Experimental determination of scanning probe microscope cantilever spring constants utilizing a nanoindentation apparatus", Rev. Sci. Instrum. 71, pp. 3769-3776, 2000

[51] http://www.hysitron.com/Products/Sellsheets/new_triboindenter.htm

[52] F.G. Zaugg, P. Wagner, "Drop-on-demand Printing of Protein Biochip Arrays", MRS Bulletin November 2003, pp. 837-842

[53] S. Kraemer, R.R. Fuierer, C.B. Gorman, "Scanning Probe Lithography Using Self-Assembled Monolayers", Chem. Rev. 103, pp. 4367-4418, 2003

[54] P. Cooley, D. Wallace, B. Antohe, "Applications of Ink-Jet Printing Technology to BioMEMS and Microfluidic Systems", Proceedings of SPIE Vol. 4560, pp. 177-188, 2001

5758-62